The Astronomical Journal, 156:66 (21pp), 2018 August https://doi.org/10.3847/1538-3881/aace5f

Revealing the Warm and Hot Halo Baryons via Thomson Scattering of Quasar Light

Lluís Mas-Ribas[1] and Joseph F. Hennawi[2,3]
[1] Institute of Theoretical Astrophysics, University of Oslo, Postboks 1029, NO-0315 Oslo, Norway; l.m.ribas@astro.uio.no
[2] Department of Physics, University of California, Santa Barbara, CA 93106, USA
[3] Max-Planck-Institut für Astronomie, Königstuhl 17, D-69117 Heidelberg, Germany
Received 2018 March 5; revised 2018 June 8; accepted 2018 June 19; published 2018 July 26

Abstract

The baryonic content and physical properties of the warm and hot ($10^5 \lesssim T \lesssim 10^7$ K) phases of the circumgalactic medium (CGM) are poorly constrained owing to the lack of observables probing the requisite range of temperature, spatial scale, halo mass, and redshift. The radiation from a luminous quasar produces a spatially extended emission halo resulting from Thomson scattering off of free electrons in the CGM, which can be used to measure the electron density profile and, therefore, the amount of warm and hot baryonic matter present. We predict the resulting surface brightness profiles and show that they are easily detectable in a three-hour integration with the *James Webb Space Telescope* (*JWST*), out to ∼100 physical kpc from the centers of individual hyperluminous quasars. This electron-scattering surface brightness is redshift independent, and the signal-to-noise ratio depends only very weakly on redshift, in principle allowing measurements of the warm and hot CGM into the Epoch of Reionization at $z \sim 6.5$. We consider a litany of potential contaminants and find that for fainter quasars at $z \lesssim 1$, extended stellar halos might be of comparable surface brightness. At $z > 2$, *JWST* mid-IR observations start to probe rest-frame optical/UV wavelengths, implying that scattering by dust grains in the CGM becomes significant, although multi-color observations should be able to distinguish these scenarios given that Thomson scattering is achromatic.

Key words: diffuse radiation – galaxies: evolution – galaxies: formation – galaxies: fundamental parameters – galaxies: halos – quasars: emission lines

1. Introduction

The circumgalactic medium (CGM) is the region extending up to a few hundreds of kiloparsecs around galaxies and where the interactions between galaxies and the intergalactic medium (IGM) take place. The gas that fuels star formation is accreted from the IGM onto the galaxy, and the material processed in the interstellar medium (ISM) can be expelled toward its outskirts in galactic winds. As the CGM constitutes the primary flow of baryonic matter in and out of galaxies, its study is crucial for understanding galaxy formation and evolution.

The rest-frame ultraviolet (UV) absorption features that the CGM gas produces in the spectra of background sources have been used to probe this medium for about half a century (see, e.g., Tumlinson et al. 2017 for a review), but advances in observational instrumentation and methodology are now also enabling detailed studies in emission (Steidel et al. 2011; Hennawi & Prochaska 2013; Cantalupo et al. 2014; Arrigoni Battaia et al. 2015; Hennawi et al. 2015). Recent observations indicate that most star-forming galaxies at high redshift show extended emission in their CGM, usually in the form of Lyα, from several tens up to ∼80–100 physical kpc (pkpc; e.g., Matsuda et al. 2012; Momose et al. 2014; Wisotzki et al. 2016; Leclercq et al. 2017; Xue et al. 2017), and often also in Hα, up to a few tens of kiloparsecs from the central stellar regions (Hayes et al. 2013; Matthee et al. 2016; Sobral et al. 2016). This diffuse emission is a new window into the structure of the CGM and can provide unique information about faint star formation in the halo of galaxies (Mas-Ribas et al. 2017a), as well as the escape of ionizing photons from galaxies into the IGM up to the redshifts of cosmic reionization (Mas-Ribas et al. 2017b). For the case of bright quasars (or active galactic nuclei, AGNs), their ionizing radiation can illuminate dense gas in their surroundings, resulting in even larger Lyα nebulosities that extend up to a few hundreds of kiloparsecs (e.g., Prescott et al. 2009; Yang et al. 2009; Hennawi & Prochaska 2013; Arrigoni Battaia et al. 2014, 2016; Cantalupo et al. 2014; Martin et al. 2014; Roche et al. 2014; Hennawi et al. 2015; Borisova et al. 2016). In extreme cases, this phenomenon can trace the densest environments, providing a signpost for the most massive (proto-) galaxies and clusters at $z \sim 2$–3 (Hennawi et al. 2015; Martin et al. 2015; Cai et al. 2017; Arrigoni Battaia et al. 2018).

The aforementioned observables provide valuable information about the medium within the temperature range $\sim 10^4$ and a few times 10^5 K (which we will hereafter refer to as the cool phase), but a complete picture of the CGM also includes gas at temperatures $10^5 \lesssim T \lesssim 10^7$ K. Hydrodynamical simulations show that the majority of the baryons interior to the virial radius of massive halos ($M_{\rm h} \gtrsim 10^{12}\, M_\odot$) are shock-heated to the virial temperature $T_{\rm vir} \gtrsim 10^6$ K (hot phase; Birnboim & Dekel 2003), but the detection of these baryons, and especially of those in the range $10^5 \lesssim T \lesssim 10^6$ K (warm phase), is difficult. Constraining the amount of warm and hot baryonic matter confined within halos is crucial to (i) gain insight into the relevance of feedback processes; if feedback effects are small, we expect most of the virialized gas to remain in the halo, whereas if feedback is important, this gas will be expelled into the IGM and mixed with the warm-hot intergalactic medium (WHIM; Cen & Ostriker 2006; Roncarelli et al. 2012; van de Voort et al. 2016). (ii) Quantifying the amount of warm and hot gas in galactic halos is important for shedding light on the so-called "missing baryons problem," which is that only a small fraction of the total baryon budget (inferred from the cosmic microwave background (CMB) and big bang nucleosynthesis) has been detected thus far (Persic & Salucci 1992; Fukugita et al. 1998; Fukugita & Peebles 2004; Tripp

et al. 2004; Prochaska & Tumlinson 2009; Shull et al. 2012). Recent studies of cosmic filaments by Tanimura et al. (2017) and de Graaff et al. (2017) suggest that $\gtrsim$30% of the missing baryons is in the WHIM, consistent with the 50% inferred from simulations by Hojjati et al. (2015), but the halo component is much more uncertain (e.g., Anderson & Bregman 2010; McGaugh et al. 2010). To assess this baryonic content, current studies typically make use of observations of the Sunyaev–Zel'dovich effect and X-rays, but these observables are not sensitive to the entire range of spatial scales, temperatures, and/or redshifts covered by the warm and hot phases of the CGM (see the review by Bregman 2007).

X-ray observations only enable studies of the hot component, at $T \gtrsim 10^6$ K, and the signal is heavily weighted toward small-scale regions because it depends on the square of the density (Gupta et al. 2012) and the metallicity (Bogdan et al. 2017; Li et al. 2017), both of which rise steeply toward the halo center. At redshifts $z \gtrsim 0.5$, the expected X-ray emission is too faint to detect galactic halos, and even at redshifts as low as $z \lesssim 0.1$, the detection is challenging. Diffuse emission from the halos of individual massive ($M_{\rm h} \gtrsim 10^{13}\ M_{\odot}$) spiral and early-type elliptical galaxies at $z \lesssim 0.1$ has been detected in a few tens of objects, but only out to a few tens of kiloparsecs from their centers (Anderson & Bregman 2011; Dai et al. 2012; Humphrey et al. 2012; Bogdán et al. 2013; Anderson et al. 2016; Goulding et al. 2016; Bogdan et al. 2017; Li et al. 2017). In most of these cases, it is challenging to separate the signal from the background beyond ~10–20 kpc, and for the compact inner emission, it is unclear whether it arises from the hot gas or is produced by faint discrete sources of stellar nature (e.g., X-ray binaries and cataclysmic processes; Bogdán et al. 2012; Dai et al. 2012). Additional sensitivity has been obtained by stacking large samples of objects, enabling detections of halo emission beyond a few hundreds of kiloparsecs from the centers of massive galaxies ($M_{\rm h} \gtrsim 10^{12.7}\ M_{\odot}$ [4]) typically residing in the centers of galaxy clusters (e.g., Anderson et al. 2013, 2015). To summarize, X-ray studies are limited to low redshifts, large masses, and hot gas, and for individual objects, to small scales around the galactic centers.

Large distances from the centers of individual massive galaxy groups and clusters can be reached by analyzing the thermal Sunyaev–Zel'dovich effect (tSZ; Sunyaev & Zeldovich 1970, 1972) that energetic free electrons in the CGM have on CMB photons. Contrary to the case of X-rays, the tSZ signal is linear in the electron density and hence less weighted toward the center. Furthermore, the tSZ effect is in principle redshift independent, although in practice size evolution and limited spatial resolution render objects at redshifts $z \gtrsim 1.5$ currently undetectable (see the reviews by Carlstrom et al. 2002 and Kitayama 2014). Individual objects (clusters) with halo masses in the range $M_{\rm h} \sim 2$–$5 \times 10^{14}\ M_{\odot}$ can be detected up to $z \sim 0.3$, and up to $z \sim 1.5$ for larger masses (Bleem et al. 2015), but stacking (or cross-correlating) thousands of objects enhances the sensitivity and, therefore, enables detections of less massive halos and higher redshifts (Scannapieco et al. 2008). The Planck Collaboration et al. (2013), Greco et al. (2015), and Ruan et al. (2015) cross-correlated tSZ maps with $z \sim 0.03$ locally bright galaxies from the Sloan Digital Sky Survey DR7 (SDSS; Abazajian et al. 2009), allowing them to assess the signal in halos of masses down to $M_{\rm h} \sim 4.4 \times 10^{12}\ M_{\odot}$. Spacek et al. (2016, 2017b) used tSZ stacks to study the environment around $M_{\rm h} \sim 7 \times 10^{13}\ M_{\odot}$ elliptical galaxies in the redshift range $z \in [0.1$–$1.5]$, and Hand et al. (2011) and Chatterjee et al. (2010) stacked the signal around $M_{\rm h} \sim 10^{14}\ M_{\odot}$ luminous red galaxies (LRGs) within $0.16 \lesssim z \lesssim 0.47$. Finally, Gralla et al. (2014) studied the tSZ signal around radio galaxies, with average halo masses $M_{\rm h} \sim 10^{13}\ M_{\odot}$ and median redshift $z \sim 1$. Overall, these studies detected average warm and hot phases broadly consistent with the amount expected from the theory for virialized galactic halos.

Stacking the tSZ signal around large samples of bright quasars allows one to characterize the properties of high-redshift halos, as well as the impact of quasar feedback on their CGM. Chatterjee et al. (2010) and Ruan et al. (2015) performed such analyses with SDSS quasars covering the redshift range $0.08 \lesssim z \lesssim 2.82$, enabling them to probe halo masses $M_{\rm h} > 10^{12.5}\ M_{\odot}$. These studies found the total thermal energy in the halos to exceed the values expected from gravitational heating by up to ~1 order of magnitude, which indicates strong contribution from feedback. However, Cen & Safarzadeh (2015) argued that the observed thermal energies can be fully explained via gravitational heating alone, given the large beam sizes of a few arcminutes for *WMAP* and *Planck*, and the uncertainties in the dust temperature in the calibration of the tSZ maps. More recently, Crichton et al. (2016) performed tSZ analyses similar to those by Chatterjee et al. and Ruan et al. with a smaller-beam experiment (ACT; ~1 arcmin; Swetz et al. 2011) and also found a large thermal energy excess, consistent with the results by Dutta Chowdhury & Chatterjee (2017), although the importance of feedback still remains under debate because of the difficulties in analyzing and interpreting the tSZ signal in all these analyses (Le Brun et al. 2015; Verdier et al. 2016; Hill et al. 2017; see also the recent findings by Spacek et al. 2017a). In detail, extracting conclusive information from observations of the tSZ effect is difficult because the separation between the actual tSZ signal and that from other contaminants, i.e., thermal radiation from dust, requires a precise (not straightforward) modeling of the emission spectrum at various frequency bands (Cen & Safarzadeh 2015; Greco et al. 2015; Ruan et al. 2015). Furthermore, the signal is unresolved at distances within the beam of the instrument and only the integrated effect, characterized by the Compton y parameter, can be measured. Finally, there is a degeneracy between the electron temperature and density, $y \propto n_{\rm e}(r) T_{\rm e}(r)$, which could vary radially and which requires additional modeling and/or assumptions (e.g., an isothermal medium) to separate these dependencies and obtain quantitative constraints.

The observation of the diffuse extended emission around a luminous quasar/AGN that results from nuclear light that has been scattered by the free electrons (Thomson scattering) in the host CGM is another potential probe of the baryons residing in galactic halos (Sunyaev 1982; Sholomitskii & Yaskovich 1990). Obvious advantages of this approach compared to other observables are: (i) this effect is sensitive to the presence of all the baryons in the halo, irrespective of their temperature, provided that they are ionized. (ii) In contrast with X-ray studies, the signal is linearly proportional to the electron density, $n_{\rm e}(r)$, resulting in a signal that decays more gradually

[4] We have converted the halo masses to the virial halo mass using the mass-conversion relations of Hu & Kravtsov (2003) when they are defined in another nomenclature.

with radius, implying potentially detectable emission at large distances. (iii) Quantifying the implied CGM density profiles is straightforward because there is no degeneracy with other parameters, in contrast with both X-ray and tSZ studies.

Because scattered radiation is also polarized (e.g., Lee 1999), electron scattering has been invoked by Antonucci & Miller (1985), Koyama et al. (1989), Miller & Goodrich (1990), Antonucci et al. (1994), Ogle et al. (2003) to explain the diffuse polarized continuum emission in the central regions ($\lesssim$1 kpc) of nearby AGNs. On larger scales, i.e., a few tens of kiloparsecs from the central source, scattering has been suggested as a potential mechanism to explain the polarization around radio galaxies at redshifts $0.5 \lesssim z \lesssim 2$ by Dey et al. (1996), Tran et al. (1998), and Cohen et al. (1999), but in these cases, it was unclear whether the scattering medium was electrons or dust (see also Kishimoto et al. 2001; Vernet et al. 2001). Geller et al. (2000) attempted to detect extended halos of polarized radio emission around a bright $z \sim 3$ radio galaxy resulting from the Thomson scattering of nuclear emission, but the limited sensitivity resulted only in weak upper limits for the halo/IGM baryon content. However, theoretical predictions by Holder & Loeb (2004) showed that modern radio interferometers may be able to detect this signal around bright radio sources inhabiting the centers of massive clusters. In view of these results, it seems that electron scattering has not yet provided competitive constraints on halo baryons because limited statistics and sensitivity imply that the majority of detections are limited to small scales, where the particle dominating the scattering process (dust or electrons) is unclear.

In principle, the nature of the scattering medium can be easily determined given a spectrum of the scattered radiation. When quasar radiation is scattered, the photons inherit a Doppler frequency shift resulting from the velocities of the scattering particles, implying that the emission lines will be broadened by thermal velocity dispersion of the scattering medium. Because this thermal line broadening scales as the scattering particle mass, $m^{-1/2}$, the large masses of dust grains will result in negligible broadening. For electron scattering, however, the resulting velocity width of scattered quasar emission lines is of the order $\gtrsim\sqrt{m_{\rm p}/m_{\rm e}}\ v_{\rm vir} = 10^4\,{\rm km\,s^{-1}}$ in massive galaxies and clusters (Loeb 1998), where $m_{\rm p}$ and $v_{\rm vir}$ are the proton mass and virial velocity, respectively, and exceeding the typical intrinsic quasar line values of $\sim 5 \times 10^3\,{\rm km\,s^{-1}}$ (Peterson 1997). This effect has been explored in the early theoretical papers of Gilfanov et al. (1987), Fabian (1989), and Sarazin & Wise (1993) to discuss the beamed AGN radiation. Because the broadening is linearly proportional to the thermal velocity of the gas, Loeb (1998) and Khedekar et al. (2014) showed that analysis of the line width can also be used to derive the electron temperature of the gas, which is a valuable complementary probe, together with the diffuse emission, to better constrain the properties of the warm and hot gas.

We propose here calculations of the extended radiation of a hyperluminous quasar scattered by the free electrons in the CGM of the host galaxy and demonstrate that this emission is a viable and unique tool to probe the properties of the warm and hot gas in the halo that is difficult to detect via other methods. The emission profiles appear to be potentially detectable with NIRCam on board the *James Webb Space Telescope* (*JWST*) and spatially resolved out to large radial scales, enabling studies of individual halos at masses lower than those in X-ray and tSZ approaches and at redshifts up to those of the cosmic reionization. Furthermore, we stress that the signal is independent of temperature and linearly proportional to electron density, enabling constraints on the total baryon content.

In Section 2, we detail the formalism for the calculation of the surface brightness profiles of electron and dust scattering, and in Section 3 we present our simple model for the medium around the quasar-host galaxy. In Section 4, we explore the potential contaminants for the scattering signal, and we detail our observational strategy in Section 5. We present the results in Section 6 and discuss our findings and approach in Section 7, before concluding in Section 8.

We assume a flat ΛCDM cosmology with the parameter values from Planck Collaboration et al. (2016).

2. Formalism

We consider a two-phase CGM, which for simplicity we call hot and cool phases, the latter containing dust, and calculate the extension of the quasar emission scattered by the free electrons and the dust in these media, respectively. Modeling the signal from dust is important given that it can potentially contaminate that from electrons.

We present in Section 2.1 the formalism for the calculation of the surface brightness profiles that result from the scattering processes of dust and electrons. In Section 2.2, we detail the calculations of the scattering redistribution function for electrons (Section 2.2.1) and dust (Section 2.2.2).

2.1. Scattering Surface Brightness Profile

The surface brightness profile at impact parameter $r_\perp$ from the central source results from integrating the radiation scattered in the host halo along the line of sight s toward the observer. The radial coordinate r is related to $r_\perp$ and s as $r^2 = r_\perp^2 + s^2$, so that $r\,dr = s\,ds$, and the surface brightness can be expressed as (Mas-Ribas & Dijkstra 2016)

$$\begin{aligned}{\rm SB}(r_\perp, \nu_{\rm obs}) &= \frac{1}{(1+z)^3}\int j(r, \nu_0) ds \\ &= \frac{2}{(1+z)^3}\int_{r_\perp}^{\infty} j(r, \nu_0)\frac{r\,dr}{\sqrt{r^2 - {r_\perp}^2}}. \end{aligned} \quad (1)$$

Here, $\nu_{\rm obs}$ is the frequency of the radiation in the observer's frame, which is related to the frequency ν_0 emitted in the rest frame of the source via $(1+z)\nu_{\rm obs} = \nu_0$, where z denotes the redshift of the source. The term $1/(1+z)^3$ results from cosmological dimming of the spectral brightness ${\rm SB}(r_\perp, \nu_{\rm obs})$ and $j(r, \nu_0)$ denotes the volumetric emissivity of the scattered radiation at frequency ν_0 and distance r, which can be further specified as

$$\begin{aligned} j(r, \nu_0) &= n_x(r)\sigma_{\rm x}\frac{L_{\nu_0}}{4\pi r^2}P_x \\ &= \tau_{x,0}\, f_{{\rm V},x}(r_{\rm vir})\frac{L_{\nu_0}}{4\pi r_{\rm vir}^3}\left(\frac{r_{\rm vir}}{r}\right)^{\alpha_x+2}P_x. \end{aligned} \quad (2)$$

The factor $1/4\pi r^2$ above accounts for the geometric dilution of the specific luminosity, L_{ν_0}, of the central source at frequency ν_0. The terms $n_x(r)$ and σ_x denote the radial volume density profile and the scattering cross-section, respectively, of the

scattering particles, and x takes on "hot" ("e"; electrons) or "cool" ("d"; dust), denoting the two CGM phases (scatterers) considered in our model (Section 3.1). The function P_x denotes the integral of the scattering redistribution function $R(\nu, \Omega)_x$ over both the solid angle Ω (between our line of sight and the original photon emission direction) and the (original) emission frequency ν, i.e., $P_x = \int\int R(\nu, \Omega)_x \, d\nu d\Omega$ (Section 2.2). We express the emissivity in terms of the scattering optical depth, $\tau_{x,0}$, considering $\tau_{x,0} = n_{x,0}\sigma_x r_{\rm vir}$,[5] and parameterizing the density as $n_x(r) = n_{x,0} f_{{\rm V},x}(r_{\rm vir})(r_{\rm vir}/r)^{\alpha_x}$, where $n_{x,0}$ and $f_{{\rm V},x}(r_{\rm vir})$ are the density and volume filling factor values, respectively, at the virial radius $r_{\rm vir}$, and α_x is the power-law index of the profile. Combining the previous two equations, the resulting surface brightness finally equals

$$\mathrm{SB}(r_\perp, \nu_{\rm obs}) = \frac{1}{(1+z)^3}\tau_{x,0} f_{{\rm V},x}(r_{\rm vir})\frac{L_{\nu_0}}{2\pi r_{\rm vir}^2} \times \int_{r_\perp}^{\infty} P_x\left(\frac{r_{\rm vir}}{r}\right)^{\alpha_x+1}\frac{dr}{\sqrt{r^2 - {r_\perp}^2}}. \quad (3)$$

We emphasize that the linear dependence of the electron-scattered surface brightness profile on the electron density is encapsulated in the optical depth, i.e., $\tau_{\rm hot} \propto n_{\rm e}$, and describe in more detail the parameters of these equations below.

2.2. Scattering Redistribution Function

For most scattering processes, the absorbed radiation is not re-emitted isotropically but rather in preferred directions that depend on the nature of the scattering medium. The probability that the scattered photons are directed along a given direction is represented by the redistribution (or phase) function $R(\nu', \boldsymbol{n}'; \nu, \boldsymbol{n})$, which denotes the probability of scattering a photon from a frequency ν' to ν and from a direction $\boldsymbol{n}'$ to $\boldsymbol{n}$ (Dirac 1925). For our purposes, the vector $\boldsymbol{n}$ will denote the direction along the line of sight toward an observer on Earth, whereas the vector $\boldsymbol{n}'$ indicates the direction of the radiation emitted by the quasar. We describe the phase function for electron scattering in Section 2.2.1 and for dust in Section 2.2.2. In all cases, we assume that the photons undergo only a single scattering event, which is a valid approximation because the CGM is optically thin to scattering by dust and electrons as shown in Section 3.1.

2.2.1. Hot CGM–Electron Scattering

For the hot phase, we consider the electron temperature to be similar to the virial temperature $T_{\rm vir} \sim 10^6$ K, implying that the free electrons are in the non-relativistic regime ($k_{\rm B}T_{\rm e} \ll m_e c^2$, where $k_{\rm B}$ denotes the Boltzmann constant, m_e is the electron mass, and c is the speed of light) and that the photon energies are below X-ray energies of 0.511 MeV, implying the low-energy scattering limit ($h_{\rm P}\nu \ll m_e c^2$, where $h_{\rm P}$ is Planck's constant). In this regime, and assuming that the free electrons follow a Maxwellian velocity distribution, the phase function is the classical Thomson redistribution function (Rybicki & Lightman 1979; Loeb 1998)[6] of the form

$$R(\nu', \boldsymbol{n}'; \nu, \boldsymbol{n})_{\rm hot} = \frac{3}{4}(1+\mu^2)\frac{1}{[2\pi\beta_T^2(1-\mu)\nu^2]^{1/2}} \times \exp\left[-\frac{(\nu-\nu')^2}{2\beta_T^2(1-\mu)\nu^2}\right], \quad (4)$$

where $\mu = \boldsymbol{n}' \cdot \boldsymbol{n} = \cos\Theta$, with Θ the angle between the vectors $\boldsymbol{n}'$ and $\boldsymbol{n}$, and $\beta_T^2 \equiv 2k_{\rm B}T_{\rm e}/m_{\rm e}c^2$, such that $\beta_T = v_{\rm th}/c$ is the electron thermal velocity in units of c. For present purposes, we will be considering observations through broad-band filters, and so the frequency redistribution will just broaden the underlying quasar spectrum by a small amount compared to the filter widths we consider. Therefore, we ignore the frequency dependence of the redistribution function and integrate between the limits of the frequency range covered by the filter[7] used in our default observational settings (Section 5), and normalize the phase function such that $\int\int C\, R(\nu', \boldsymbol{n}'; \nu, \boldsymbol{n})_{\rm hot}\, d\nu\, d\Omega = 1$, where C is a normalization constant.

The top-left panel in Figure 1 displays the electron redistribution function with $\mu = \cos\Theta$, showing that the forward- and back-scattering scenarios are favored ($\mu = 1$ and $\mu = -1$, respectively), while the lowest probability is for $\mu = 0$ ($\Theta = 90°$ between the incoming and outgoing photon directions). Forward scattering is slightly more favored than the backward one. The bottom-left panel represents the probability of scattering a photon into the line of sight toward the observer for every position in a plane intersecting the quasar host, defined by $\boldsymbol{n} \times \boldsymbol{n}'$, the vector normal to the plane, where $\boldsymbol{n}$ defines the direction toward the observer, and $\boldsymbol{n}'$ is the direction of ray of radiation emitted by the quasar. The middle-left panel shows the projection along the line of sight ($\boldsymbol{n}$) of the 2D distribution, which will be the relevant quantity for the surface brightness calculation. Because forward and back scattering are preferred, this leads to the projection of the redistribution function peaking at small impact parameters, because at these distances, most of the contribution comes from photons emitted in the direction parallel (or antiparallel) to the observer. At large impact parameters, the line-of-sight integral has a much greater contribution from photons emitted at intermediate angles, which have a lower probability of scattering toward the observer.

2.2.2. Cool CGM–Dust Scattering

For the cool phase, we consider the scattering by the dust particles embedded in this medium. The Henyey–Greenstein function (Henyey & Greenstein 1941) is usually used to describe the anisotropic scattering phase function of a mixture of dust grains, but Draine (2003) proposed an improved function to better match the real one at wavelengths $\lambda > 1\ \mu$m. We adopt the dust redistribution function from Draine (2003),

$$R(\mu)_{\rm cool} = \frac{1}{4\pi}\frac{1-g^2}{1+\alpha(1+2g^2)/3}\frac{1+\alpha\mu^2}{(1+g^2-2g\mu)^{3/2}}, \quad (5)$$

[5] In detail, the quantity $\tau_{x,0}$ represents the differential optical depth at the virial radius, as $\tau_x(R) = \int_0^R d\tau_x(r) = \int_0^R n_x(r)\sigma_x dr$. We use this term as a parameterization and avoid the differential notation for simplicity.

[6] While our equation is adequate for our purposes, we refer the interested reader to Sazonov & Sunyaev (2000) for a detailed and comprehensive work on the redistribution function for high-energy photons and semi-relativistic cases.

[7] We have ignored the filter curve in this integral as this would mostly only change the normalization constant.

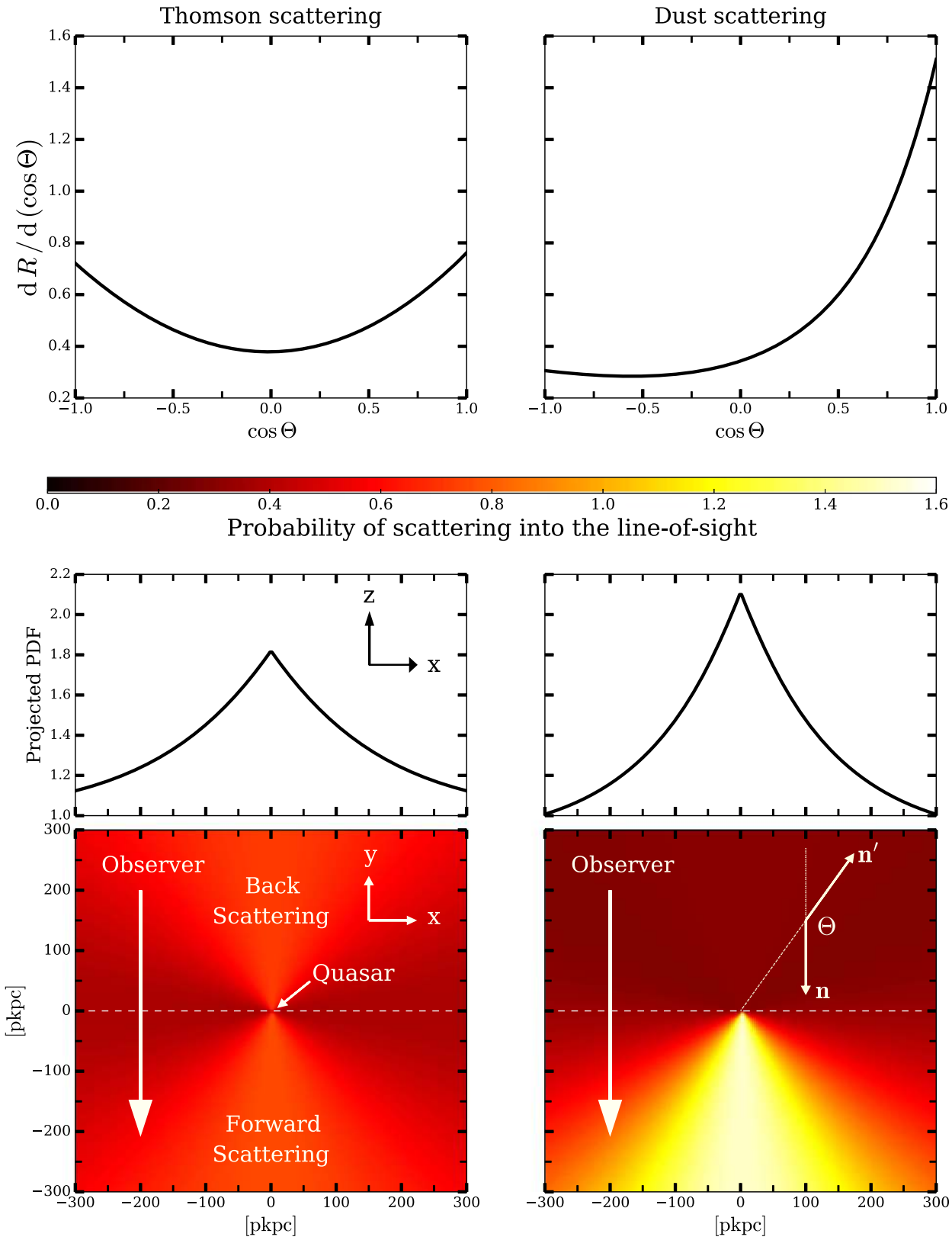

Figure 1. Nature and impact of the scattering redistribution functions of non-relativistic free electrons (left column) and dust (right column). The top panels represent the redistribution functions with $\cos\Theta$, where Θ is the angle between the incoming and outgoing photon. The right panel shows the preference for forward scattering for the case of dust. The lower panels display the probability distribution functions of scattering photons toward the observer at every position of a plane $\boldsymbol{n} \times \boldsymbol{n}'$ containing the quasar in the center. The middle panels show the previous distributions projected along the observer's line of sight, indicating that the highest projected probability of scattering photons toward the observer is found at small impact parameters from the quasar. In the bottom-right panel, we illustrate an example of the angle Θ between the line of sight and the radial vector for a given position of the plane.

with the parameters $g = 0.26$ and $\alpha = 0.62$. These parameter values result from considering a Milky Way dust model and radiation at $\lambda = 1.2\,\mu$m (lower panel of Figure 6 in Draine 2003), consistent with our approach for dust (next section) and our proposed observational setup (Section 5). Considering these parameters and the term $1/4\pi$ in Equation (5), this function does not require further normalization.

The dust redistribution function is plotted in the top-right panel of Figure 1, which shows the strong preference of dust for scattering the radiation in the same direction as the incoming photons (forward scattering), maximizing the probabilities at angles $|\Theta| \lesssim 30°$. The favored forward-scattering scenario is clearly observed in the 2D PDF plot in the bottom-right panel of Figure 1, appearing as a bright triangular area in the lower half of the plot, while the upper part, representing back scattering, is almost homogeneously dark. This dust property results in a more sharply peaked projected probability profile compared to that of electrons (middle-right panel).

3. Parameterization of the Host CGM

In this section, we describe how we model the physical properties of the CGM of the host galaxy (Section 3.1), which we use to compute 2D maps of scattered quasar emission (Section 3.2).

3.1. Host Galaxy CGM

We consider a two-phase halo, consisting of a hot CGM phase composed of hot plasma that has been shock-heated to the halo virial temperature and is collisionally ionized (Section 3.1.1) and a cool (dusty) CGM component, characterized in the works of the Quasars Probing Quasars series by Hennawi et al. (2006), Hennawi & Prochaska (2007), Prochaska & Hennawi (2009), and Lau et al. (2016), and by Lyα emission constraints from the work by Arrigoni Battaia et al. (2016; see Section 3.1.2 in this paper).

3.1.1. Hot CGM Phase

We model the distribution of hot gas as

$$n_{\rm H,hot}(r) = n_{\rm H,hot,0}\, f_{\rm V,hot}(r_{\rm vir}) \left(\frac{r}{r_{\rm vir}}\right)^{-\alpha_{\rm h}}, \tag{6}$$

where we assume a volume filling factor $f_{\rm V,hot}(r_{\rm vir}) = 1$, the term $\alpha_{\rm h} = 5/2$ is derived from the hydrodynamical simulations by Nelson et al. (2016), and $n_{\rm H,hot,0}$ is the volume density of hydrogen in the hot phase at the virial radius, obtained as follows. In Nelson et al., the dark matter halos with mass $M_{\rm h} \sim 10^{12}\,M_\odot$ at $z = 2$ have a virial radius $r_{\rm vir} \sim 100$ pkpc and a gas density $n_{\rm H,0} \sim 10^{-3.75}\,{\rm cm}^{-3}$, which we use to calculate the hot gas mass enclosed within their virial radius as $M_{\rm vir,hot} = 4\pi\, n_{\rm H,0}\, f_{\rm V,hot}(r_{\rm vir}) r_{\rm vir}^3 / (3 - \alpha_{\rm h})/X$, with $X = 0.76$ denoting the cosmic hydrogen abundance. The ratio between the hot and total baryonic mass is then obtained using the cosmic baryon fraction, $f_{\rm b} = \Omega_{\rm b}/\Omega_{\rm m} = 0.174$, resulting in $M_{\rm vir,hot}/(f_{\rm b} M_{\rm h}) = 0.83$, which we fix for our further calculations. In practice, variations in redshift, halo mass, galaxy type, etc., may change the value of the ratio, but we expect the halo of massive quasar hosts to be dominated by hot gas in any case, as indicated by simulations (e.g., Birnboim & Dekel 2003; Nelson et al. 2016). We have checked that variations of this value by $\lesssim$25% do not greatly alter our conclusions. Finally, we obtain $n_{\rm H,hot,0}$ by solving the above equations using now the fixed ratio; a halo mass $M_{\rm h} = 10^{12.5}\,M_\odot$, characteristic of dark matter halos hosting quasars (White et al. 2012; see also Conroy & White 2013); and the corresponding virial radius for this halo mass at the redshift of interest.

This hot phase contains free electrons that will scatter the quasar radiation. We parameterize the Thomson-scattering optical depth by these free electrons with the quantity $\tau_{\rm hot,0} = n_{\rm e,0}\sigma_{\rm e} r_{\rm vir}$, where $\sigma_{\rm e} = \sigma_T \equiv 6.65 \times 10^{-25}\,{\rm cm}^2$ is the Thomson-scattering cross-section, and $n_{\rm e,0} = (1 + Y/2X) n_{\rm H,hot,0}$ is the electron volume density at $r_{\rm vir}$, with $Y = 0.24$ denoting the cosmic helium abundance. In general in our calculations, the photons reaching the CGM have traversed an electron-scattering optical depth with a value of $\sim 10^{-2}$, consistent with the typical value of the intracluster medium. This optical depth represents an optically thin medium to electron scattering that ensures the validity of the single-scattering approximation in our calculations. We ignore the scattering driven by dust in this phase because we expect a dust-to-gas mass ratio far below 1% (Laursen 2010 and references therein).

3.1.2. Cool CGM Phase

We characterize the cool CGM phase with a population of $T \sim 10^4$ K spherical gas clouds of uniform density, $n_{\rm H,cool,0}$, distributed in the halo according to a radial volume filling factor of the form (Hennawi & Prochaska 2013)

$$f_{\rm V,cool}(r) = f_{\rm V,cool}(r_{\rm vir}) \left(\frac{r}{r_{\rm vir}}\right)^{-\alpha_{\rm c}}, \tag{7}$$

where $f_{\rm V,cool}(r_{\rm vir})$ is the volume filling factor at the virial radius, and α_c is the power-law index of the density scaling relation in this medium. Similarly, the density distribution of cool gas with radial distance from the center can be expressed as

$$n_{\rm H,cool}(r) = n_{\rm H,cool,0}\, f_{\rm V,cool}(r_{\rm vir}) \left(\frac{r}{r_{\rm vir}}\right)^{-\alpha_{\rm c}}. \tag{8}$$

Given these assumptions, the average column density of cool gas at impact parameter $r_\perp$ is obtained as

$$\begin{aligned}\langle N_{\rm H,cool}(r_\perp)\rangle &= \int_{r_\perp} n_{\rm H,cool}(r)\, ds \\ &= 2 N_{\rm H,cool,0} \sqrt{\left(\frac{r_{\rm max}}{r_{\rm vir}}\right)^2 - \left(\frac{r_\perp}{r_{\rm vir}}\right)^2} \left(\frac{r_\perp}{r_{\rm vir}}\right)^{-\alpha_h} \\ &\quad \times {}_2F_1\left[\frac{1}{2}, \frac{\alpha_h}{2}, \frac{3}{2}, 1 - \left(\frac{r_{\rm max}}{r_\perp}\right)^2\right],\end{aligned} \tag{9}$$

where $r_{\rm max} = 2\, r_{\rm vir}$ is the maximum radius out to which the profile in Equation (8) extends, $N_{\rm H,cool,0}$ denotes the cool gas column density at the virial radius, and the term ${}_2F_1$ is the Gaussian hypergeometric function that accounts for the integral along the line of sight at a given impact parameter. A similar expression to Equation (9) holds for the mean column density

of the hot phase, $\langle N_{\rm H,hot}(r_\perp)\rangle$, provided we replace $\alpha_{\rm c}$ by $\alpha_{\rm h}$ and $N_{\rm H,cool,0}$ by $N_{\rm H,hot,0}$.

We set $\alpha_{\rm c}=0$ owing to the weak radial dependence of $N_{\rm H}$ on the impact parameter out to $\approx$200 kpc, obtained by Lau et al. (2016) from the photoionization modeling of a sample of $z\sim 2$–3 background quasar sightlines passing through the CGM. Because we previously obtained that 83% of the baryonic mass is in the hot gas, we determine the degenerate product $n_{\rm H,cool,0}\, f_{\rm V,cool}\,(r_{\rm vir})$ from the expression $M_{\rm vir,cool}=4\pi n_{\rm H,cool,0}\, f_{\rm V,cool}\,(r_{\rm vir})\,(\, r_{\rm vir}^3/(3-\alpha_{\rm c})/X$ by assuming that the remaining 17% of the mass is in the cool phase. This calculation results in a value of the column density at the virial radius of $N_{\rm H,cool,0}\sim 10^{20}\,{\rm cm}^{-2}$, broadly consistent with the results by Lau et al. (2016) and Prochaska & Hennawi (2009).

The scattered emission from the cool phase is driven by the presence of dust in the CGM, which has been inferred at large radial distances, from several tens of kiloparsecs up to several megaparsecs from the centers of $z\sim 0.3$ SDSS galaxies by Ménard et al. (2010; see also Peek et al. 2015). We quantify the dust-scattering optical depth assuming that the dust-to-gas ratio scales as the CGM metallicity compared to the solar value, $Z_\odot$, with a ratio $Z/Z_\odot=1/10$ (Prochaska et al. 2013) and a reddening parameter $R_{\rm V}=3.1$, the value typically considered for the ISM of the Milky Way with a column density $\sim 2\times 10^{21}\,{\rm cm}^{-2}$. Using these parameters and our cool gas column density results in a reddening

$$E(B-V)=\frac{Z}{Z_\odot}\,\frac{N_{\rm H,cool,0}}{2\times 10^{21}\,{\rm cm}^{-2}}\sim 10^{-2},$$

in agreement with the weak evidence for reddening of SDSS quasars reported by Krawczyk et al. (2015; see also Richards et al. 2003). We adopt the Milky Way extinction curve by Cardelli et al. (1989), which gives the attenuation curve A_λ, because it extends into the near infrared (NIR; considered for our observations), although the curve for the Small Magellanic Cloud (SMC) might be a more accurate choice given the low metallicity of the CGM (Hutchings 1982; Laursen 2010; Peek et al. 2015). However, we have tested that extrapolating the SMC law by Gordon et al. (2003) to the NIR does not alter our results. We set the dust albedo (the probability that a photon is scattered instead of destroyed by dust) to $a_{\rm d}=0.7$, consistent with the values by Li & Draine (2001) and Draine (2003). Finally, the dust optical depth parameter equals

$$\tau_{{\rm cool},0,\lambda}=a_d\,A_\lambda\,\frac{R_{\rm V}}{3.1}\,\frac{Z}{Z_\odot}\,\frac{N_{\rm H,cool,0}}{2\times 10^{21}\,{\rm cm}^{-2}},$$

which, considering the rest-frame NIR wavelengths of our fiducial calculations, results in dust optical depths of the order 10^{-5}, about three orders of magnitude smaller than that of electrons.

3.2. Maps of Scattered Emission

Once the parameterization of the CGM and the redistribution functions are established, we can calculate the emissivity of radiation scattered into the line of sight toward the observer at every position of the halo. The bottom panels in Figure 2 display this spatial distribution in the plane defined by $\boldsymbol{n}\times\boldsymbol{n}'$ for electrons (left panel) and dust (right panel). The colors indicate the value of the emissivity at every point of the plane, with brighter colors denoting higher values. The left panel shows a distribution elongated along the line of sight, driven by the preference of Thomson scattering for forward and back scattering, with the signal decreasing with impact parameter from the center. The right panel indicates that most of the signal arises from radiation scattered between the quasar and the observer, at small angles from the line of sight ($\lesssim 60^\circ$), resulting from the forward-scattering redistribution function pattern of dust. Most of the radiation emitted at larger angles does not contribute to the observed signal, except for scatterings occurring close to the center ($r\lesssim$ 50–70 pkpc). The upper panels show the surface brightness profiles resulting from integrating the scattered emissivity of the lower 2D maps along the line of sight toward the observer (i.e., Equation (1)). For this calculation, we have used the parameters of the central source that we detail in Section 5. Briefly, we have considered the rest-frame radiation at 1.8 μm from a hyperluminous quasar at $z=1$, with an apparent magnitude in the i band of 15.5 mag.

4. Other Sources of Diffuse Halo Emission

The electron-scattering surface brightness profile could be potentially confused with the signal from dust, but also with other sources of diffuse emission from the halo of the host galaxy. We thus also estimate the potential contamination from the nebular emission resulting from the interaction between the quasar radiation and the cool CGM gas in Section 4.1, and that from star formation in the host galaxy in Section 4.2.

4.1. Extended Nebular Emission

We estimate the level of nebular emission in the halo, which arises from the interaction between the radiation of the central quasar and the cool gas. We use the photoionization code CLOUDY v10.01, last described by Ferland et al. (2017), and follow the method by Arrigoni Battaia et al. (2015, their Sections 4.3 and 4.4), for which we briefly describe the main steps below. We use the quasar spectral energy distribution (SED) described in Section 5 for our adopted central source as input to CLOUDY to parameterize the radiation field illuminating the CGM and the values for the cool CGM phase detailed in the previous sections to characterize the gas. Given the small size of the cool clouds compared to their distance from the central source (more than $\sim$50 times larger), we assume a plane-parallel geometry for the computations. The output from CLOUDY is the emissivity j_ν arising from the cool clouds at various distances from the central source, from which we compute the surface brightness at various impact parameters using Equation (1). Despite its simplicity, this calculation is enough to ensure that the nebular emission is not a contaminant of the electron-scattered signal in the first 150–200 pkpc. We show the nebular surface brightness profile, together with those of dust and electrons, in Section 6.1.

4.2. Stellar Emission

Stellar emission in the quasar-host halo could be a significant contaminant of the electron-scattering signal. We estimate the impact of this effect accounting for the signal from possible extended stellar halos in Section 4.2.1 and that from satellite galaxies clustered around the central source in Section 4.2.2.

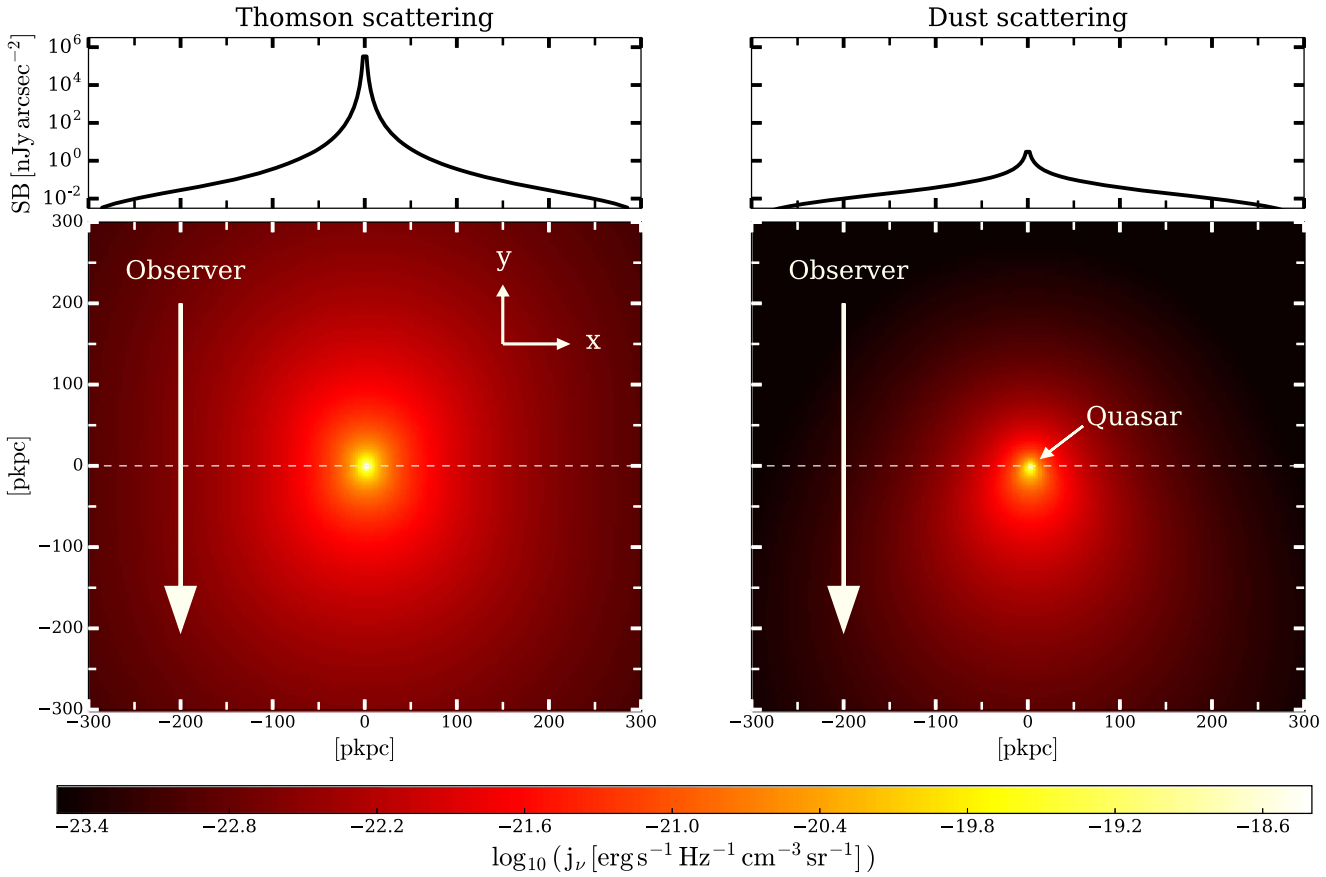

Figure 2. Bottom panels: two-dimensional maps of quasar radiation scattered into the line of sight toward the observer at every point of the $\boldsymbol{n} \times \boldsymbol{n}'$ plane. The left panel illustrates the elongated distribution of scattered emission driven by the Thomson-scattering redistribution function. The right panel shows the preference of the dust redistribution function for forward scattering, which favors the emission from the scattering sites placed at small impact parameters from the central quasar. Top panels: surface brightness profiles of the lower panels integrated along the line of sight for each case.

4.2.1. Extended Stellar Halos

Observations of massive $\log(M_{\rm h}/M_\odot) \gtrsim 12.5$–13 early-type elliptical galaxies at redshifts $z \lesssim 1$ show extended stellar halos that can be individually detected out to several tens of kiloparsecs (e.g., Schombert 2015; Buitrago et al. 2017; Huang et al. 2017; Oh et al. 2017) and up to a few hundreds of kiloparsecs when stacking a large number of them (e.g., Kormendy et al. 2009; Tal & van Dokkum 2011; D'Souza et al. 2014) with radial profiles significantly flatter than those of other types of galaxies, e.g., spirals, that typically have more compact stellar components (e.g., Courteau et al. 2011). The origin of these extended stellar halos is an unsolved problem, but it has been suggested that they arise from the rapid growth of the progenitor galaxies at redshifts $z \sim 2$–4 (e.g., Dekel et al. 2009), followed by the quenching of star formation driven by stellar and/or AGN feedback (see Harrison 2017 for a review), and a final period (at $z \lesssim 1$) of non-dissipative merger events with other galaxies (Conroy et al. 2007; Purcell et al. 2007; Szomoru et al. 2012; Patel et al. 2013).

The diffuse emission from these extended stellar halos could be comparable to the electron-scattering signal if the quasar host resembles a massive elliptical galaxy, which is often the case for luminous quasars at low redshift ($z \lesssim 1$; e.g., Guyon et al. 2006; Hyvönen et al. 2007a, 2007b; Veilleux et al. 2009). However, observational characterization of these extended stellar surface brightness profiles is challenging because it often requires assumptions about the intrinsic ellipticity of the galaxy, complex subtraction of contaminant neighboring and/or foreground sources, as well as modeling of the the point-spread function (PSF) of the observations (Abraham et al. 2017; Knapen & Trujillo 2017). Because observations of extended stellar halos are available at low redshift where they are also expected to be larger, we estimate the intensity of this signal in our discussion of the electron-scattering emission from the quasar 3C 273 at $z \sim 0.16$ in Section 6.3.1.

4.2.2. Satellite Galaxies

The presence of faint galaxies around the quasar can be another potential contaminant to the scattering emission. If these galaxies are individually detectable, they can be masked and removed from the images, but, otherwise, we cannot separate their contribution from the diffuse halo emission. For the case of undetectable galaxies along the line of sight but far from the host halo, we expect their distribution to be uncorrelated with the quasar, and therefore their emission is effectively part of the sky background which will be subtracted from images of the quasar. However, faint (undetectable) galaxies clustered around the central quasar produce a signal that cannot be masked and which will not subtract out. Recent studies have indicated that the clustering of galaxies around quasar hosts is significant (e.g., Coil et al. 2007; Trainor & Steidel 2012; Wang et al. 2015; Decarli et al. 2017; Garcia-Vergara et al. 2017). Thus, the collective, azimuthally integrated emission from these clustered satellite sources can

produce diffuse light in the host halo, as we discussed in Mas-Ribas & Dijkstra (2016) and Mas-Ribas et al. (2017a), which could masquerade as the scattering signal we are interested in. Below we estimate the size of this effect.

The first step in this calculation is to obtain the luminosity (magnitude) above which satellite galaxies clustered around the central quasar can be individually detected, and therefore removed, given our observational setup. We discuss the observational strategy in detail in Section 5, but we briefly present the essential details here. We consider observations using the NIRCam instrument on board the *JWST* (Gardner et al. 2006), with the broadband filter F356W, which covers the spectral region where the sky background is minimum. The default exposure time is set to 7200 s, and we assume the quasar-host halo to be at redshift $z = 1$. This redshift implies NIR emission is observed from the sources (centered at $\sim$1.8 μm in the source rest frame), a region of the galaxy spectrum dominated by stellar continuum light. We consider a source to be detectable when its signal is, at least, five times the value of the noise σ, with $\sigma = \sqrt{N_{\rm sky} + {\rm RN}^2}$. Here, $N_{\rm sky}$ and ${\rm RN} = 2$ are the photon counts for the sky brightness and instrumental readout noise, respectively, detailed in the next section. In the calculation of the sky photon count, we have considered an effective area for the satellite galaxies $S_{\rm eff} = \pi r_{\rm eff}^2$, where $r_{\rm eff} = 0.5$ arcsec is the galaxy radius. We plug these numbers into Equation (12) and obtain the minimum flux of a detectable galaxy, i.e., our detection threshold, resulting in $m_{\rm AB} \sim 28.3$ AB apparent magnitudes, broadly consistent with the sensitivity estimates in the NIRCam documentation.[8]

As shown below, our calculations result in an average number of $\sim$0.25 undetectable satellite galaxies in the halo, which imply highly stochastic surface brightness values that depart strongly from the deterministic average profile. We assess the impact of the satellites using a Monte Carlo approach to better capture this effect, instead of using the analytical approach that we adopted in Mas-Ribas et al. (2017a), where we analytically computed the mean (field) emissivity of the faint galaxy population and boosted its value close to the central source using the correlation function. In detail, we now perform 10^6 realizations where, in each of them, we populate the host halo with satellite galaxies by randomly sampling the luminosity and correlation functions that describe the satellite population. When a satellite galaxy is above our detection threshold, we consider it to be detectable and able to be masked out, and we do not add it to the halo. Therefore, each realization is a possible scenario illustrating the impact of the undetectable satellite sources on the scattering surface brightness profiles. We characterize the parameters of the luminosity function for satellite sources by using the fitting formula in Stefanon & Marchesini (2013, their Section 4.2) at redshift $z = 1$, which is constrained at the rest-frame H band ($\sim$1.6 μm), consistent with the rest-frame wavelength of our observations. The absolute magnitude of our detection threshold then corresponds to $M_{\rm H,thr} = -15.9$ mag assuming a negligible K-correction (Poggianti 1997; Mannucci et al. 2001), and the parameters of the luminosity function, $\phi_{\rm H}(M)$, are $M_{\rm H}^* = -23.88$ mag, $\phi_{\rm H}^* = 1.1 \times 10^{-3}\,{\rm mag}^{-1}\,{\rm Mpc}^{-3}$, and power-law index $\alpha_{\rm H} = -1.15$. The observed magnitudes in Stefanon & Marchesini (2013) cover the range $-M_{\rm H} \sim 18$–26 mag, but we extend these limits for our calculations. We set the upper limit of the integral over the luminosity function to $M_{\rm H,max} = -27$ mag for numerical purposes, although the exact value is irrelevant given that these satellites are above the detection threshold and will not be considered. For the lower limit, we integrate down to $M_{\rm H,min} = -12$ mag, accounting for possible undetected galaxies not captured in the luminosity functions by Stefanon & Marchesini (2013). We have tested that variations around this limit do not alter our results because the faint-end slope of the luminosity function is significantly flat.

In order to model the clustering of satellites around the central quasar, we use the power-law cross-correlation function between galaxies and quasars at $z = 1$ reported by Coil et al. (2007), $\xi^{\rm GQ}(r) = (r/r_0^{\rm GQ})^{\gamma^{\rm GQ}}$, with scale length $r_0^{\rm GQ} = 3.3\,h^{-1}$ cMpc and power-law index $\gamma^{\rm GQ} = -1.55$. We divide our range of magnitudes into 35 bins, resulting in variations $dM_{\rm H} = 0.43$ mag, and the radial distances between $r_{\rm min} = 20$ kpc and $r_{\rm max} = 300$ kpc into 19 evenly distributed logarithmic bins, resulting in $d\log(r/{\rm kpc}) = 0.06$. The lower limit for the radial distance is set by considering that the possible effect of the quasar-host galaxies is not captured by our simple method. The chosen number of bins allows us to precisely sample the distributions while not slowing down the computations; we have tested that the results are insensitive to the exact number of bins. We finally populate the halos following the steps described below:

1. We calculate the exact number of galaxies at every radial bin i with the expression

$$n_i = \int_{M_{\rm H,min}}^{M_{\rm H,max}} \phi_{\rm H}(M)\,dM \int_{r_i}^{r_{i+1}} 4\pi r^2\,[1 + \xi^{\rm GQ}(r)]\,dr, \quad (10)$$

   where the first integral provides the mean number density of galaxies in the field, and the second enhances this number according to the radial cross-correlation function and integrates it over the volume of the bin.
2. For every radial bin, we sample a Poisson distribution centered at the values n_i to obtain an integer number of galaxies. In most iterations, the total number of galaxies in the bins, and in the whole halo, is zero because the average number of galaxies per bin fluctuates within the range $10^{-2} \gtrsim n_i \gtrsim 10^{-5}$, and the total number of undetectable galaxies in the halo is 0.25. If the total number of galaxies is null, we repeat this step considering a new realization.
3. If the previous step results in one or more galaxies, we then assign them a luminosity (magnitude) by using the inverse cumulative distribution function (ICDF) sampling method applied to the luminosity function $\phi_{\rm H}(M)$. If the magnitude assigned to the galaxy is smaller (the galaxy is brighter) than our detection threshold, we remove this galaxy from the calculation and do not consider it further. If all galaxies are discarded because they are detectable and maskable, we return to step 2.
4. If there are undetectable satellite galaxies, we place them in the host halo. The radial distance is set by the radial bin the galaxies belong to, and we specify the positions on a sphere centered at the quasar using two angles, Θ and Φ, obtained by randomly drawing values from the ranges $2\pi \gtrsim \Theta \gtrsim 0$ and $\pi/2 \gtrsim \Phi \gtrsim -\pi/2$. We then project the

[8] https://jwst-docs.stsci.edu/display/JTI/NIRCam+Imaging+Sensitivity (Figure 1, scaled to our 5σ value)

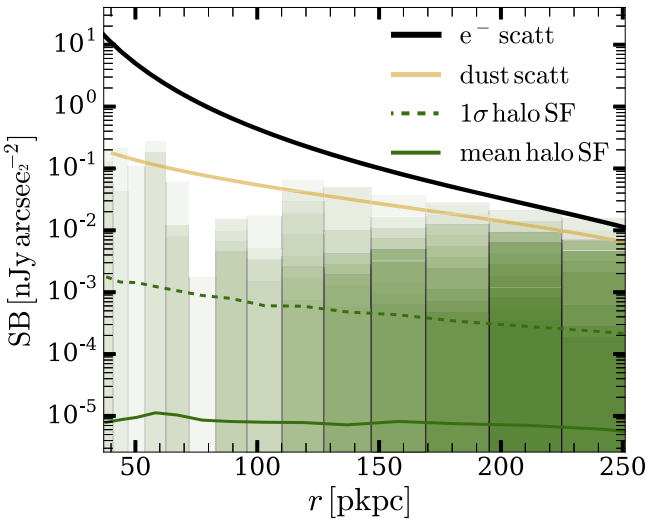

Figure 3. Surface brightness profiles from Figure 2, for electron (black line) and dust scattering (orange line). Each green bar denotes the surface brightness introduced by one undetectable satellite galaxy at its corresponding projected distance bin, typically representing one realization. The image shows around a thousand realizations overplotted, where in most cases the number of satellites is null. Most of the satellites reside within ∼150–250 kpc and show surface brightness levels below the electron signal. The signal from satellites is $\gtrsim$1 decade below that from electrons at projected distances $r \lesssim 100$ pkpc. The solid and dashed green lines represent the mean and one-sigma deviation, respectively, of the surface brightness profile from satellites (halo star formation, SF) after 10^6 realizations. A publicly available movie at https://github.com/lluism/QSO_scattering shows the iterative procedure for visualization.

position of the undetectable satellites onto the plane perpendicular to the line of sight to obtain the impact parameter of each source.

5. Finally, we transform the magnitude of every satellite to flux density and divide it by the area of the radial annulus where the projected galaxies are placed, thus obtaining the surface brightness values.

Figure 3 illustrates the impact of the undetectable satellite sources on the electron- (black line) and dust- (orange line) scattering surface brightness profiles from Figure 2. Every vertical green bar represents the surface brightness introduced by one undetectable satellite galaxy at its corresponding (projected) radial bin, after computing and overplotting 1000 realizations. In ∼75% of the realizations, there are no undetectable satellites and, when present, they mostly reside in the range within ∼150–250 kpc from the center. At $r \lesssim 100$ pkpc, the electron-scattering surface brightness level is generally more than one order of magnitude higher than the brightest undetected sources, and the electron-scattering profile dominates the signal out to ∼200 pkpc. The solid and dashed green lines denote the mean and standard deviation values, respectively, of the surface brightness profiles for the undetected satellites after the full calculation with 10^6 realizations. We stress that these profiles are much fainter than the typical surface brightness value introduced by the individual satellites because ∼75% of the realizations contribute to the calculation with zero satellites, i.e., null surface brightness, driven by the average number of 0.25 galaxies per halo. Finally, the contamination will generally only affect one spurious impact parameter bin as this is the typical value of satellites per halo when they are present, which implies that satellite sources are not a strong contaminant to the overall electron-scattering profile. Given this result, we do not consider the effect of satellites in our further calculations. A publicly available movie at https://github.com/lluism/QSO_scattering shows the iterative procedure for visualization.

5. Observational Strategy

This section presents a detailed discussion of our observational approach, which aims to maximize the signal-to-noise ratio (S/N) of the electron-scattered quasar radiation.

We consider the Near Infrared Camera (NIRCam) on board *JWST*. The large aperture of *JWST* (25 m^2) provides higher sensitivity to low surface brightness emission than the *Hubble Space Telescope* (*HST*), and its well-characterized PSF guarantees that regions contaminated by the central hyperluminous quasar emission will be minimized. Our primary setup uses the broadband filter F356W, centered at 3.568 μm with bandwidth BW = 0.781 μm. We choose this filter in particular because it is broad, and the S/N scales as S/N $\propto$ BW$^{1/2}$ (Equations (11) and (12)), and the central wavelength of F356W coincides with the region where the sky background is the faintest. This is clear from the lower panel of Figure 4, which shows the NIRCam broadband filters superposed on a plot of the surface brightness of the *JWST* sky background versus wavelength from Krick et al. (2012).[9]

To maximize the S/N of the electron-scattering halo, we will target a hyperluminous quasar. For the choice of redshift, we choose $z = 1$ as our fiducial value, motivated by the following points: (i) at lower redshifts, the possible presence of extended stellar halos around the host galaxy could be a significant contaminant of the electron-scattering signal. Indeed, we show that this could be an issue for a hypothetical observation of 3C 273 at $z = 0.16$, which we discuss in detail in Section 6.3.1. We expect the amplitude of the extended stellar halo emission to be smaller at higher redshifts, $z \gtrsim 1$, due to lower stellar masses and $(1+z)^4$ surface brightness dimming. (ii) The metallicity of the gas, directly related to the expected amount of dust, is higher at lower redshifts, thus enhancing the possible dust contamination. (iii) Given the well-known strong luminosity evolution of quasars with increasing redshift, there are already hyperluminous quasars at $z \sim 1$ that are an order of magnitude brighter than the brightest local quasars like 3C 273 ($z = 0.158$). (iv) Finally, at $z \sim 1$, our filter covers the rest-frame NIR region of the quasar spectrum (see Figure 4), whereas at $z \gtrsim 2$ it shifts into the optical/UV, which increases the dust-scattering optical depth relative to the electron-scattering optical depth, resulting in potential contamination from dust scattering as well as from nebular radiation. In this case, the effect of dust is not due to the variation of the amount of dust but to the wavelength dependence of its absorption cross-section, which is much larger at optical/UV wavelengths than at longer NIR wavelengths. The contamination from nebular radiation is also most important when observing in the UV range, because many bright hydrogen and metal recombination lines (as well as continuum) are present. We analyze the redshift dependence of the electron-scattering emission in more detail in Section 6.2.

In order to maximize the S/N of the electron-scattering signal, we wish to target hyperluminous quasars, generally found at high redshift (e.g., Boyle et al. 1988), with their number density peaking at $z \sim 2$ and decreasing rapidly at

[9] https://jwst-docs.stsci.edu/display/JPP/JWST+Backgrounds

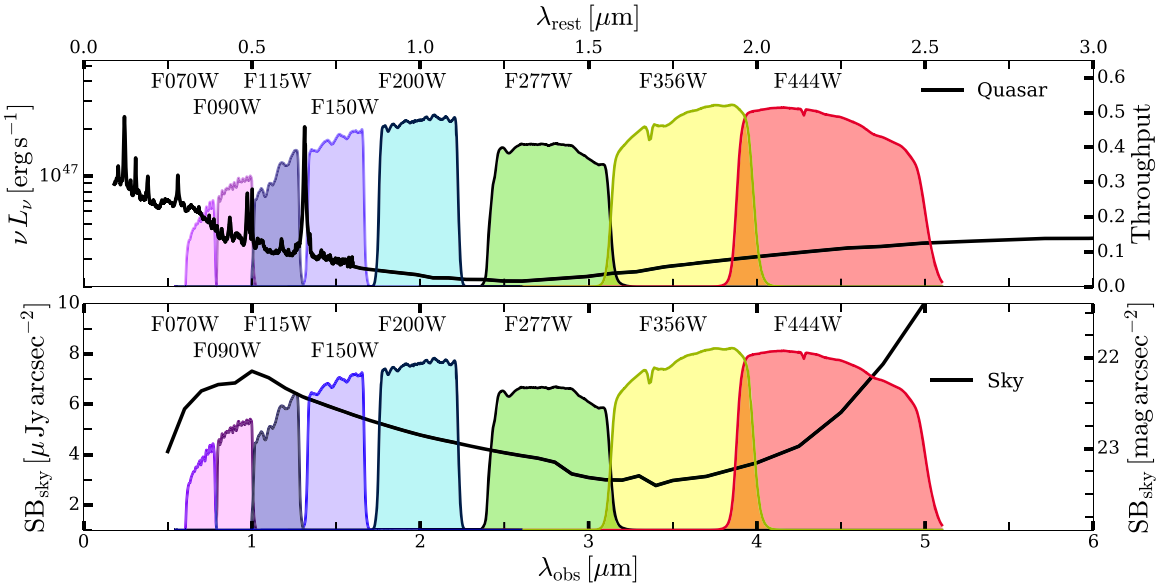

Figure 4. Upper panel: quasar SED at the observer and source ($z = 1$) frames, with broadband NIRCam filters superposed on it. The left axis denotes the quasar luminosity and the right axis the total system throughput considering each filter. Lower panel: surface brightness with wavelength for the background sky.

higher redshift (Boyle et al. 2000; Wu et al. 2010). Stern et al. (2015) analyzed large samples of quasars and found that the brightest objects (in terms of apparent magnitude) generally inhabit the range $1 \lesssim z \lesssim 1.5$. These objects have i-band apparent magnitudes of $\sim$15.5 mag, which we adopt as our intrinsic quasar brightness. We compute the SED of this hyperluminous quasar following the procedure described in Arrigoni Battaia et al. (2015). Specifically, redward of the Lyman limit, we model the spectrum by splicing together the composite spectra by Lusso et al. (2015), Vanden Berk et al. (2001), and Richards et al. (2006a) and normalizing the amplitude to obtain the desired magnitude. The template by Richards et al. (2006a) is the most relevant for our calculations because we focus on the rest-frame NIR range of the quasar spectra. For energies above 1 Rydberg, which we have used for our nebular calculations with CLOUDY, we make use of power laws: from 1 to 30 Rydberg, we assume a power law $L_\nu = L_{\nu_{\rm LL}}(\nu/\nu_{\rm LL})^{\alpha_{\rm UV}}$, with $\nu_{\rm LL}$ and $L_{\nu_{\rm LL}}$ denoting the frequency and luminosity at the Lyman limit, respectively, and $\alpha_{\rm UV} = -1.7$. Above 30 Rydberg and up to 2 keV, we change the power-law index to -1.65, and to -1 for the X-ray band from 2 to 100 keV. Above this value, the hard X-ray slope is set to -2 (see Arrigoni Battaia et al. 2015 for details on these calculations and references). The upper panel in Figure 4 displays the quasar SED in the rest and observer frames, with the NIRCam wideband filters superposed on the spectrum. The vertical right axis denotes the total system throughput considering each of the filters.

Finally, using the aforementioned parameters, the detectability of the electron-scattering signal can be quantified. In all that follows, we assume an exposure time of 10^4 s. The S/N and the corresponding observational uncertainties for the electron-scattered surface brightness profile are computed according to

$$\mathrm{S/N} = N_s/\sqrt{N_s + N_{\rm sky} + RN^2 + N_{\rm PSF}}. \quad (11)$$

Here, N_s and $N_{\rm sky}$ are the azimuthally integrated photon number counts for the electron-scattered radiation and sky background, respectively, calculated from

$$N = \frac{f(\nu_{\rm obs})}{h_{\rm p}} \frac{\rm BW}{\lambda_{\rm obs}} A_{\rm aper}\, \eta\, t_{\rm exp}, \quad (12)$$

where $h_{\rm p}$ is Planck's constant, $\lambda_{\rm obs} = (1+z)\lambda_0$ is the observed-frame wavelength corresponding to the center of the filter, $A_{\rm aper} = 25$ m^2 corresponds to the *JWST* aperture, and η is the total system throughput, which is shown on the upper-right axis of Figure 4. The term $f(\nu_{\rm obs}) = \int {\rm SB}(r_\perp, \nu_{\rm obs}) dA_{r_\perp}$ is the source or sky flux density (in Jansky) computed by integrating the surface brightness profile within the area $dA_{r_\perp}$ of logarithmically spaced radial annuli. The term $N_{\rm PSF}$ represents the photon count from the PSF, calculated using `WebbPSF`[10] and convolved with the total flux within the filter, assumed to be emitted by a point source. This term arises from considering the subtraction of the PSF in the analysis with a residual equal to 1% of its total value. In practice, it represents the possible fluctuation between the actual PSF photon count and the average PSF determined in the subtraction. Because of the compactness of the *JWST* PSF compared to large radii, one would conclude, for the electron-scattering signal, that the noise contributed by the PSF term is small, and thus the details of PSF subtraction, and the potential systematics associated with it, are not a significant concern.

6. Results

The surface brightness profiles resulting from our calculations are presented in Section 6.1, and in Section 6.2 we discuss the dependence of the detectability on redshift. An application of our formalism and the comparison to observations of the low-redshift quasar 3C 273 is performed in Section 6.3.1, and the profiles of the high-redshift quasar SDSS J152156+520238 are estimated in Section 6.3.2.

[10] http://webbpsf.readthedocs.io/en/latest/#

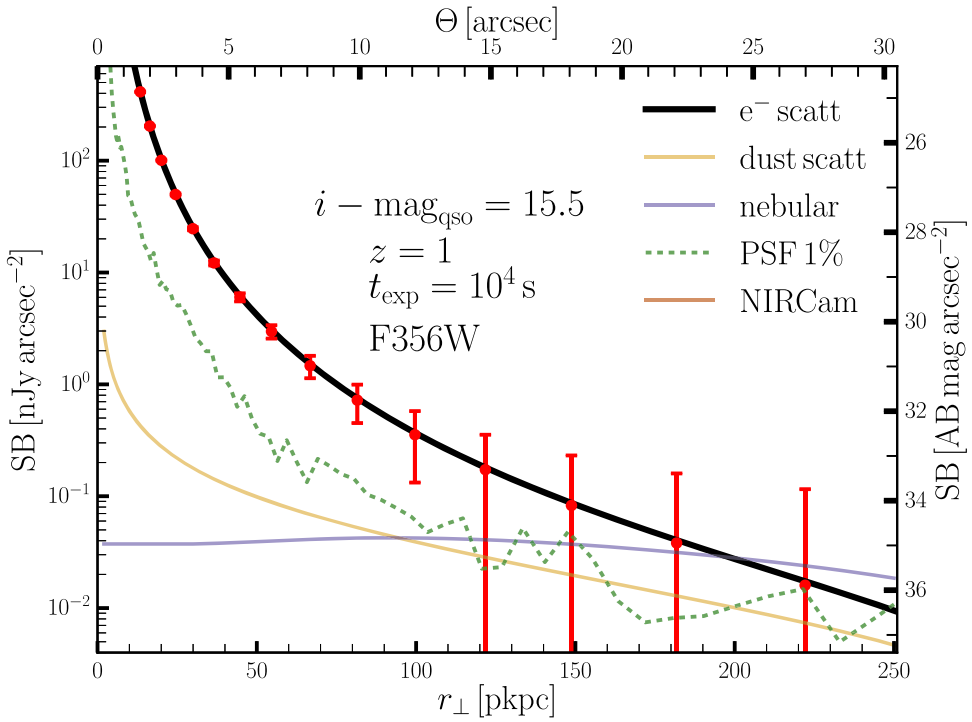

Figure 5. Radial surface brightness profiles from the central quasar, for electron-scattered radiation (black line), dust-scattered radiation (orange line), and nebular emission from the cool gas (blue line) around the host galaxy. The dashed green line denotes the residual profile of the PSF assuming that it is subtracted down to 1% of its total value. The red error bars represent the observational uncertainty derived from the S/N, calculated assuming an exposure time of 10^4 s (<3 hr) with NIRCam on board *JWST*, with the broadband filter F356W, implying the observation of the quasar rest-frame NIR. This result indicates that the electron-scattered signal is detectable, and distinguishable from the other components, up to ∼100 pkpc from the center (beyond the PSF).

6.1. Surface Brightness Profiles and Detectability

Figure 5 illustrates our predicted surface brightness profiles and the expected S/N for a hyperluminous quasar at $z = 1$. The electron-scattering profile is denoted by the black line and is clearly above the dust (orange line) in the first hundred physical kiloparsecs from the center of the host galaxy. The vertical red error bars indicate the uncertainty in the NIRCam observations of the electron-scattered radiation, where the signal appears to be detectable (S/N >1) out to ∼100 pkpc (down to ∼32.5 mag arcsec^{-2}) from the center of the quasar host with an exposure of 10^4 s (2.78 hr). The dashed green line represents the profile of the filter PSF reduced down to 1% of its original considering the PSF subtraction. Increasing the exposure time to 10 hr would allow a detection above the noise to be obtained out to ∼150 pkpc. The blue line represents the nebular radiation resulting from the interaction between the radiation field of the quasar and the cool gas in the CGM as described in Section 4.1. We have tested that using the filters F444W (resulting in a higher electron-scattering signal but also a larger sky background) or F322W2 (extra broad, covering the range with minimum sky background, i.e., ∼2.5–4 μm; Figure 4) does not significantly alter the results. This nebular component is not a significant contaminant of the electron profile below ∼150–200 pkpc, and neither is the average profile of the satellite sources, the level of which resides roughly two decades below the vertical scale of Figure 5. Due to the small impact of satellites and nebular radiation, we henceforth consider only the electron- and dust-scattering profiles.

6.2. Redshift Evolution of the Signal

The dependence of the electron-scattering emission S/N on redshift is assessed in this section. In what follows, we focus on cosmological scaling and will apply our formalism to two specific hyperluminous quasars and discuss other effects, such as contamination from extended stellar halos and dust, in the next section.

First, we derive a simple analytical expression to gain insight into the evolution of the electron-scattering surface brightness and its detectability with redshift. We consider the surface brightness, SB($r_\perp$), resulting from the integration of the specific surface brightness from our previous calculations over a fixed observed-frame filter bandwidth $\Delta\nu_{\mathrm{obs}} = \nu_{\mathrm{obs},2} - \nu_{\mathrm{obs},1}$, where the two frequencies denote the filter limits,

$$\begin{aligned}\mathrm{SB}(r_\perp) &= \int_{\nu_{\mathrm{obs},1}}^{\nu_{\mathrm{obs},2}} \mathrm{SB}(r_\perp, \nu_{\mathrm{obs}}) d\nu_{\mathrm{obs}} \\ &= \frac{1}{(1+z)^3}\tau_{\mathrm{hot},0}\frac{1}{2\pi r_{\mathrm{vir}}^2} C(r_\perp/r_{\mathrm{vir}}) \int_{\nu_{\mathrm{obs},1}}^{\nu_{\mathrm{obs},2}} L_{\nu_0} d\nu_{\mathrm{obs}},\end{aligned} \tag{13}$$

where $C(r_\perp/r_{\mathrm{vir}})$ is a geometric factor that depends only on the radial profile slope of the hot gas α_h. Assuming now a constant SED, i.e., $L_{\nu_0}\nu_0 = \mathrm{const}$, and noting that

$$\begin{aligned}\int_{\nu_{\mathrm{obs},1}}^{\nu_{\mathrm{obs},2}} L_{\nu_0} d\nu_{\mathrm{obs}} &= \int_{\nu_{\mathrm{obs},1}/(1+z)}^{\nu_{\mathrm{obs},2}/(1+z)} \frac{L_{\nu_0}}{1+z} d\nu_0 \\ &= \frac{L_{\nu_0}\nu_0}{1+z}\ln(\nu_{\mathrm{obs},2}/\nu_{\mathrm{obs},1}) \approx \frac{L_{\nu_0}\nu_0}{1+z}\frac{\Delta\nu_{\mathrm{obs}}}{\nu_{\mathrm{obs}}},\end{aligned} \tag{14}$$

we arrive at

$$\mathrm{SB}(r_\perp) = \frac{C(r_\perp/r_{\rm vir})}{(1+z)^4}\tau_{\rm hot,0}\frac{L_{\nu_0}\nu_0}{2\pi r_{\rm vir}^2}\frac{\Delta\nu_{\rm obs}}{\nu_{\rm obs}}. \quad (15)$$

Thus, the surface brightness due to electron scattering scales as the usual $(1+z)^{-4}$ from cosmological surface brightness dimming times the quantity $\tau_{\rm hot,0}/r_{\rm vir}^2 \propto n_e/r_{\rm vir}$. Because the electron density $n_e \propto (1+z)^3$ and the virial radius $r_{\rm vir} \propto (1+z)^{-1}$ (ignoring the other weak redshift dependencies in the equation for $r_{\rm vir}$), we see that $\tau_{\rm hot,0}/r_{\rm vir}^2 \propto (1+z)^4$. Thus, the electron-scattering $\mathrm{SB}(r_\perp)$ is redshift independent. The fact that the gas density increases with redshift as $(1+z)^3$ and that the virial radius, which quantifies the size of the high-redshift shock-heated regions, decreases as $r_{\rm vir} \propto 1/(1+z)$ cancels out the cosmological effect of surface brightness dimming.

Next, we assess our ability to detect the electron-scattering signal with redshift. Assuming for simplicity that the detectability is background limited (i.e., $N_{\rm sky}$ dominates the noise in Equation (11)), and integrating the surface brightness over both frequency and the angular aperture enclosing the source, we obtain

$$\int \mathrm{SB}(r_\perp, \nu_{\rm obs}) d\nu_{\rm obs} d\Omega \approx \mathrm{SB}(r_\perp)\Delta\Omega, \quad (16)$$

where $\Delta\Omega \simeq (r_{\rm vir}/D_A)^2$, and D_A denotes the angular diameter distance. Combining with Equation (11),

$$\mathrm{S/N} \propto \frac{\mathrm{SB}(r_\perp)}{\sqrt{\mathrm{SB}_{\rm sky}(r_\perp)}}\sqrt{\Delta\Omega} \propto \frac{\mathrm{SB}(r_\perp)}{\sqrt{\mathrm{SB}_{\rm sky}(r_\perp)}}\left(\frac{r_{\rm vir}}{D_A}\right). \quad (17)$$

Thus, for a fixed-luminosity (flat spectrum) source, the $\mathrm{SB}(r_\perp)$ is redshift independent, and the S/N scales as the angular size of the object, $\Delta\theta_{\rm vir} = r_{\rm vir}/D_A$. This calculation was idealized in that we adopted a flat spectrum source and imagined integrating over a fixed observed-frame frequency range. It thus ignores the fact that the range of rest-frame frequencies that one probes shifts blueward with increasing redshift. Nevertheless, it illustrates the the main dependencies with redshift.

We now more accurately calculate the values of the S/N for the electron-scattered emission at different redshifts and compare them with our analytical results. We consider our default *JWST* filter F356W, an exposure time of 10^4 s, and the projected distance bin $0.3 \leqslant r_\perp/r_{\rm vir} \leqslant 1$ in order to avoid the area contaminated by the central source PSF. We assume a constant dark matter halo mass of $\log M_{\rm h}[M_\odot] = 12.5$ and compute the corresponding virial radius at each redshift. The purple line in Figure 6 represents the S/N evolution with redshift for quasars with a constant UV absolute magnitude $M_{1450} \simeq -29$ mag, consistent with the brightest SDSS quasars in Richards et al. (2006b) and Stern et al. (2015) at redshifts $z > 1.3$. The dashed line illustrates the evolution of the ratio $r_{\rm vir}/D_A$ expected from our analytical calculation, normalized such that the two curves coincide at $z = 4$ for comparison. The steep rise of the signal at $z < 1$ is driven by the behavior of the angular diameter distance and enhanced by the $(1+z)^{-1}$ redshift scaling of the virial radius. At higher redshifts, $z \gtrsim 1.5$, the angular diameter distance begins to mildly decrease with increasing redshift, resulting in a flatter evolution. The differences between the purple and dashed lines arise from the fact that for each redshift our filter observes different parts of the rest-frame quasar spectrum, and the quasar SED increases toward bluer wavelengths (Figure 4). The cyan line in Figure 6 denotes the S/N considering the brightest observed quasars, listed in Table 1, with their M_{1450} absolute magnitudes indicated in the plot. The two solid curves follow well our predicted evolution (dashed line), enabling the measurement of the electron-scattered quasar emission up to the redshifts of cosmic reionization at $z \sim 6.5$. Despite the low brightness ($M_{1450} = -28.6$ mag) of the $z = 4.5$ quasar, the S/N appears as high as that of brighter objects because the strong Hα emission line falls at the center of our filter in this case. The blue gradient in Figure 6 illustrates the potential contaminant emission arising from the extended stellar halos inhabiting the quasar-host galaxies, which appears to be important at redshifts $z \lesssim 1$ (see next section). The orange gradient represents the impact of dust scattering on the electron-scattering signal with redshift, which starts being important in our models at $z \sim 2.5$–3 (see Section 6.3.2). The strength of the color in the gradients illustrate qualitatively the potential increase of the effects of the contaminants.

In the next section, we perform detailed calculations for real objects at low and high redshifts, and further explore the impact of potential contaminants.

6.3. Application to Real Quasars

Here we apply our formalism to two real hyperluminous quasars, the radio-loud source 3C 273 at $z = 0.158$ in Section 6.3.1 and the quasar SDSS J152156+520238 at $z = 2.208$ in Section 6.3.2, and compare the results.

6.3.1. 3C 273 and Extended Stellar Halos

The radio-loud quasar 3C 273 (Schmidt 1963) is a well-studied nearby source, placed at $z = 0.158$ (749 Mpc), with brightness $M_{\rm V} = -26.7$, and a bright extended radio jet (e.g., Uchiyama et al. 2006). The host is an elliptical E4 galaxy with (at least) four neighboring galaxies within 150 pkpc (Bahcall et al. 1997; see the review by Courvoisier 1998).

Images of the inner parts of 3C 273 in most frequency bands appear saturated due to the brightness of the quasar. Therefore, studies of the host demand the use of coronagraphs to mask the central source (e.g., Martel et al. 2003) and accurate modeling and subtraction of the PSF (Bahcall et al. 1995; Hutchings et al. 2004), which requires the *HST*'s compact and stable PSF. Martel et al. (2003) used the *HST* Advanced Camera for Surveys (ACS) coronagraph to obtain surface brightness profiles out to ∼25 kpc (∼9 arcsec) in the *I*, *V*, and *g* bands. Their observations suggested the presence of an extended stellar halo around the host galaxy, with no evidence of blue, young star-forming regions, and morphology similar to that of elliptical galaxies at large radii, but with a possible spiral structure and signatures of a merging event close to the center.

Here, we compare our calculations of the electron- and dust-scattering surface brightness profiles with the observations of 3C 273 by Martel et al. To get a handle on the expected extended spatial profile of the stellar emission, we also compare the average (stacked) surface brightness profile of massive SDSS early-type galaxies by D'Souza et al. (2014) and the deep observations of a local spiral by Trujillo & Fliri (2016).

Because the observational data cover the wavelength range ∼0.6–0.8 μm, we now calculate the scattering profiles considering the NIRCam filter F070W, centered at 0.7 μm, and corresponding to a quasar rest-frame wavelength of ∼6000 Å, and adopt an exposure time of 15 minutes. For 3C

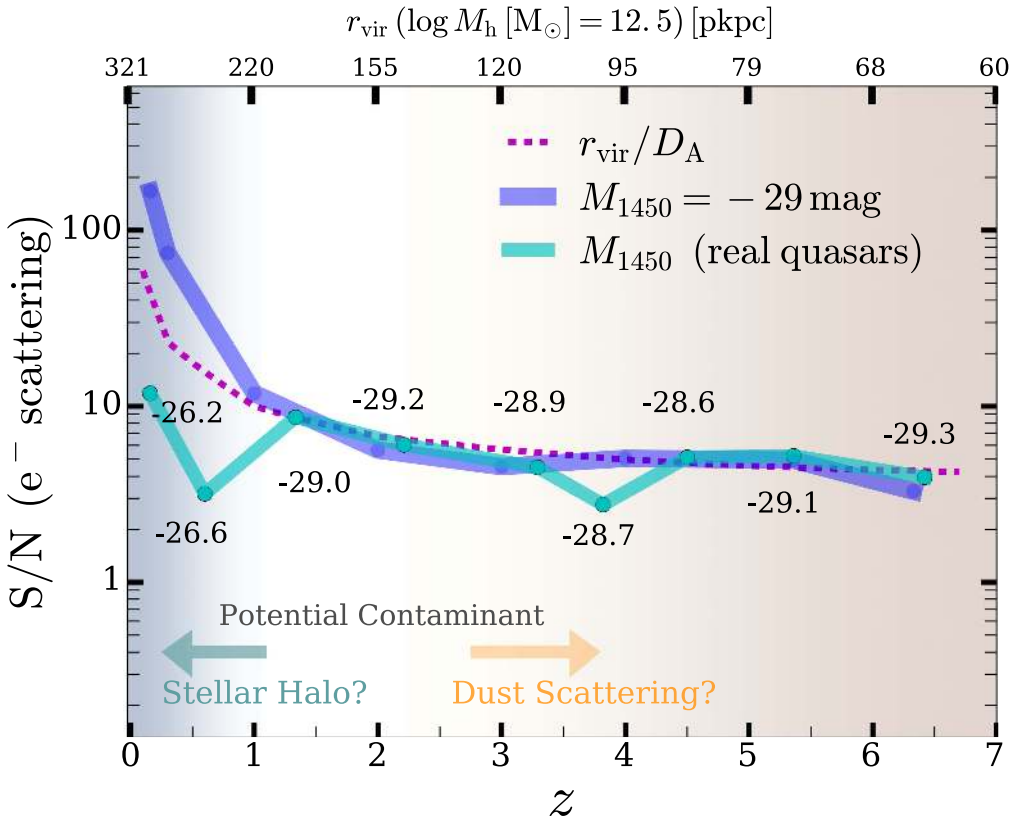

Figure 6. Dependence of the detectability (expressed as the S/N) on redshift for the electron-scattered emission, considering the default *JWST* NIRCam filter F356W, an exposure time of 10^4 s, and the projected distance bin $0.3 \leqslant r_\perp/r_{\rm vir} \leqslant 1$. The purple line denotes the evolution for a fixed quasar brightness of $M_{1450} = -29$ mag, consistent with the absolute magnitudes of the brightest quasars in Stern et al. (2015) and Richards et al. (2006b) at $z > 1.3$, and the dashed line represents our analytical prediction as $r_{\rm vir}/D_{\rm A}$, normalized to match the purple line at $z = 4$ for comparison. The cyan line shows the evolution for the brightest observed quasars, listed in Table 1, with their absolute magnitudes M_{1450} shown in the plot. The detectability depends weakly on redshift, which allows measurements of the electron-scattered emission up to the Epoch of Reionization at $z \sim 6.5$. The blue gradient illustrates the potential contaminant emission from extended stellar halos inhabiting the quasar-host galaxies, important at redshifts $z \lesssim 1$, and increasing with color strength toward lower redshifts. The orange gradient qualitatively represents the increasing impact of dust scattering on the electron-scattering signal with redshift, which starts being important in our models at $z \sim 2.5$–3. We have assumed a constant dark matter halo mass of $\log M_{\rm h}[M_\odot] = 12.5$, and computed the corresponding virial radii at each redshift, shown in the upper horizontal axis.

Table 1
Observed Quasars

Quasar	z	M_{1450} (mag)	References[a]
3C 273	0.158	−26.2	1
SDSS J210001.24-071136.3	0.600	−26.6	2
PG 1634+706	1.334	−29.0	2
SDSS J152156.48+520238.5	2.208	−29.2	2
SDSS J090033.50+421547.0	3.290	−28.9	2
SDSS J163909.10+282447.1	3.819	−28.7	2
SDSS J134743.29+495621.3	4.510	−28.6	2
SW J030642.51+185315.8	5.360	−29.1	3
SW J010013.02+280225.8	6.326	−29.3	4

Note.
[a] Sources: (1) Soldi et al. (2008), (2) Stern et al. (2015), (3) Wang et al. (2016), (4) Wu et al. (2015).

273's SED, we use the fitting profile from Soldi et al. (2008), which extends from ultraviolet to millimeter wavelengths (green line in their Figure 5). We use this spectrum because it is specific for this object, but we have checked that using our default quasar template does not result in significant differences.

The black and orange lines in the left panel of Figure 7 denote the computed electron- and dust-scattering emission profiles, respectively, and the red error bars the expected uncertainties in *JWST* measurements. The gray squares extending out to ∼9 arcsec (∼25 kpc) represent the *HST*/ACS F814W (*I* band) observations of 3C 273 by Martel et al. (2003) without applying any correction, which are significantly above the expected scattering signals at impact parameters $\gtrsim$15 kpc.

To obtain a more general comparison that extends out to larger radii, we also show the profile resulting from the stacking of massive SDSS early-type galaxies in the *r* band from D'Souza et al. (2014). We select their stack of galaxies inhabiting the redshift range $0.06 \leqslant z \leqslant 0.10$, the stellar mass range $M_* \sim 10^{11}$–$10^{11.4}\,M_\odot$, and concentration parameter $C > 2.6$, which represents high-mass isolated central galaxies (Wang & White 2012), with ellipticity consistent with that of the LRG galaxy sample in Tal & van Dokkum (2011; typical central ellipticals in galaxy groups). This profile is represented by the violet crosses and appears brighter than that of the electron scattering by a factor of around 5 at impact parameters $\gtrsim$50 pkpc, suggesting that the extended stellar halo of low-z massive early-type galaxies, if present, can in fact dominate the extended emission. We plot the data by D'Souza et al. below the first 100 pkpc from the center, because the uncertainty in the profile beyond this point rapidly becomes very large and possibly limited by systematics in their stacking procedure.

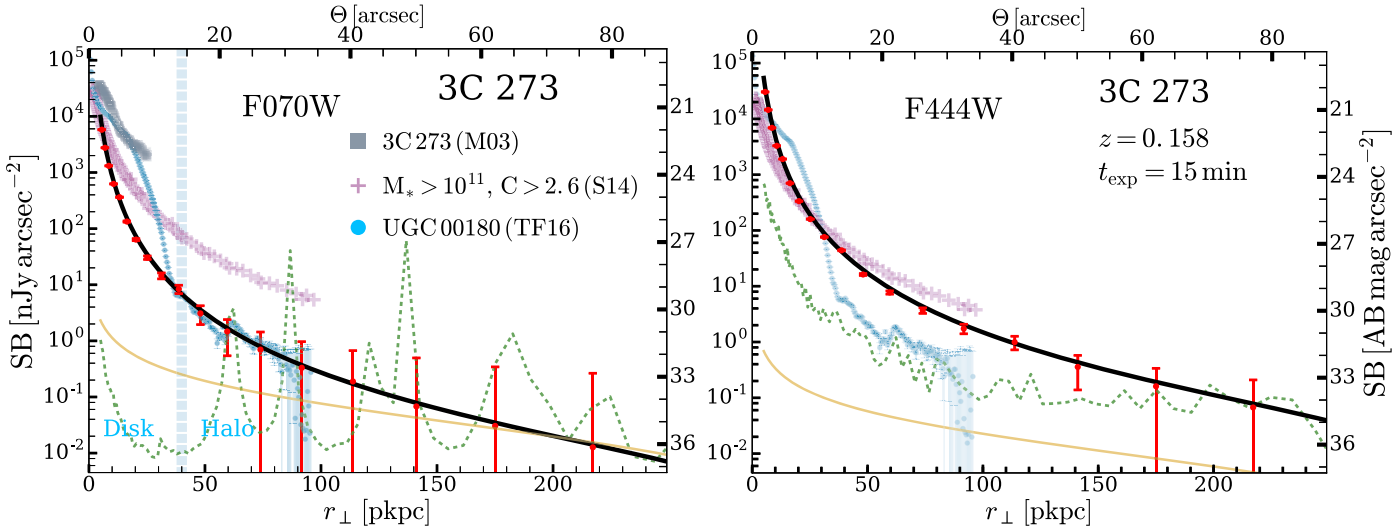

Figure 7. Surface brightness profiles for the radio-loud galaxy 3C 273. Left panel: electron-scattering (black line), dust-scattering (orange line), and 1% PSF profiles as in previous figures but considering the NIRCam filter F070W, centered at 0.7 μm, 15 minutes of exposure time, and the 3C 273 continuum-only quasar spectrum template of Soldi et al. (2008). The gray squares denote the *HST*-ACS F814W (*I* band) coronagraph data of 3C 273 by Martel et al. (2003), and the violet crosses the *r*-band stack of SDSS galaxies in the ranges $0.06 \leqslant z \leqslant 0.10$, $M_* \sim 10^{11}$–$10^{11.4}\,M_\odot$, and with concentration parameter $C > 2.6$ by D'Souza et al. (2014), consistent with isolated elliptical galaxies. We plot the D'Souza et al. data in the first 100 pkpc, where the uncertainties are small compared to the signal. For comparison, the blue data show the profile of the spiral Sab galaxy UGC 00180 observed in the *r* band by Trujillo & Fliri (2016), corrected by redshift dimming. The vertical blue line denotes the separation between the disk and the halo of UGC 00180 proposed by Trujillo & Fliri. Right panel: same as in the left panel but with calculations performed at 4.4 μm, with the filter F444W, and where we have corrected for the variation of the flux with wavelength (see text). In general, the stellar halo profiles appear as a potential contaminant at this low redshift.

Because 3C 273 does not belong to a galaxy group, and given the evidence for spiral structure in the inner parts of its host galaxy (Martel et al. 2003), we also compare to the profile for the spiral (Sab) galaxy UGC 00180 observed in the *r* band by Trujillo & Fliri (2016), representing one of the deepest observations of extended emission around local galaxies. The galaxy UGC 00180 is similar to the Andromeda galaxy (M31), with a stellar mass of $M_\star \sim 1.3 \times 10^{11}\,M_\odot$ and at $z = 0.0369$. In this case, we correct the original Trujillo & Fliri data for the $(1+z)^4$ surface brightness dimming effect due to the different redshifts of the sources, and we plot it as blue points and error bars. The UGC 00180 profile is higher than that of electrons for the first ∼30 kpc and comparable at larger distances. This transition point corresponds to the separation between the disk and the halo of UGC 00180 (dashed vertical line) noted by Trujillo & Fliri. In view of this comparison, we conclude that the signal from spiral galaxies can overwhelm that of electron scattering in the central regions of the galaxy. In the halo, even though the stellar halo of spirals is typically fainter than for ellipticals, it can still reach levels comparable to the electron-scattering signal.

We perform a similar comparison, now considering the mid-IR part of the quasar spectrum. We wish to observe the reddest possible part of the galaxy spectrum, where the possible contamination from nebular radiation is expected to be smaller than in the previous calculation and the rest-frame wavelength corresponds to the Rayleigh–Jeans tail of the stellar emission, thus reducing the impact of the extended stellar halo. For this purpose, we use the broadband filter F444W, centered at 4.4 μm, corresponding to the quasar rest-frame wavelength of ∼3.8 μm, and the same values as before for the other parameters. These scattering profiles are shown in the right panel of Figure 7. The violet crosses indicate the profile for elliptical galaxies from D'Souza et al. (2014), but now correcting the D'Souza et al. *r*-band measurements to values appropriate for mid-IR observations with F444W. Specifically, we assume that the average SED of the D'Souza et al. galaxy sample is well represented by the spectrum of the elliptical E4 galaxy (same type as 3C 273) NGC 0584 in Brown et al. (2014, their Figure 9), which covers the wavelength range of interest, ∼0.15–30 μm. According to the SED by Brown et al., $\lambda_{r\text{-band}}\, f_{r\text{-band}} / \lambda_{4.4}\, f_{4.4} = 10$, which we use to rescale the D'Souza et al. measurements to 4.4 μm. To obtain the specific surface brightness, however, we have to also account for the change in wavelength so that $\mathrm{SB}_{\nu,4.4} = \lambda_{r\text{-band}}/\lambda_{4.4}\, \mathrm{SB}_{\nu,r\text{-band}}$, altogether resulting in small variations of the stellar halo surface brightness profile compared to that in the left panel (∼26%). This small difference between the surface brightness at the two wavelength ranges considered here is consistent with the findings by Temi et al. (2008), who found similar surface brightness levels for the mid-infrared *J*, *H*, *K*, and 3.6, 4.5, 5.8, and 8.0 μm passbands in the stack of 18 local elliptical galaxies. Interestingly, these authors also found that the surface brightness differences between bands remain almost constant with the distance from the center of the galaxy (their Figure 2). The corrected surface brightness profile from D'Souza et al. still overlaps with that of electrons, indicating that emission from an extended stellar halo could still dominate even at the reddest mid-IR wavelengths. The blue points and error bars show the data for UGC 00180 from Trujillo & Fliri (2016), again corrected for the difference in redshift and now also rescaled to 4.4 μm. For the latter, we use the SED of the Sa spiral galaxy NGC 5953 in Brown et al., which indicates that $\lambda_{r\text{-band}}\, f_{r\text{-band}} / \lambda_{4.4}\, f_{4.4} = 8$. This analysis suggests that the electron-scattering emission should dominate over the stellar emission at distances $\gtrsim$25–30 pkpc from the center, if the galaxy hosting 3C 273 is a spiral galaxy like UGC 00180.

In conclusion, for the brightest nearby quasar 3C 273, the presence of a stellar halo appears to be a potential contaminant for the electron-scattering signal, but large variations in the

stellar surface brightness profiles, as well as in the shape of the spectra between galaxies of the same type, can exist (e.g., Mannucci et al. 2001), and detailed analyses, which are beyond the scope of our current work, should be carried out to assess the detectability of other low-z quasars. Note, however, that while 3C 273 has a large apparent magnitude, $i \simeq 13$ mag, its absolute magnitude is just $M_{1450} = -26.2$ mag (using the Soldi et al. 2008 et al. SED fit), which is a factor of ∼30 fainter than the hyperluminous quasars at $z > 1$, which have $M_{1450} \simeq -29$ mag (see Figure 6). Thus, given that extended stellar halos are comparable to the expected electron-scattering surface brightness at $z \sim 0.16$ around 3C 273, we expect the extended stellar emission to be much fainter than electron scattering at higher redshifts for two reasons. First, at higher z, the (rest-frame) extended stellar halo surface brightness will be at most comparable to (and possibly lower than) what we have assumed for 3C 273, under the plausible assumption that this emission scales with the M_* of the host galaxy, given the high values of $M_* \sim 10^{11}\,M_\odot$ that we considered in Figure 7 and that stellar masses are lower at higher redshift. But the quasars at higher z are ∼30 times brighter, boosting the electron-scattering signal by the same factor. Second, whereas the extended stellar halo emission will redshift away due to the strong $(1+z)^{-4}$ scaling of cosmological SB dimming, we showed in Section 6.2 that the electron-scattering surface brightness is redshift independent. In summary, although extended stellar emission will likely complicate efforts to detect electron-scattering emission from 3C 273, we expect contamination from stars to be much less important around hyperluminous quasars at $z > 1$. Lastly, we note that even at $z < 1$, it should be straightforward to assess whether extended stellar halos are a significant contaminant by simply obtaining images of fainter quasars for which the electron-scattering signal is expected to be undetectable.

Finally, we stress that while Thomson scattering is wavelength independent, the optical depth to scattering by dust particles for shorter wavelength (UV) photons is much higher than at redder IR wavelengths, due to the increase of the dust absorption cross-section with decreasing wavelength (e.g., Pei 1992). This effect is visible in Figure 7, where the dust surface brightness in the right panel (F444W probing rest frame 4 μm) is between a factor of ∼4–5 lower than in the left panel (F070W probing rest frame ∼6000 Å). Observing the rest-frame IR is thus beneficial to minimize the undesired contamination by dust.

6.3.2. Hyperluminous Quasars at $z \gtrsim 2$

We now estimate the scattering surface brightness profiles for the hyperluminous SDSS quasar J152156.48+520238.5 at redshift $z = 2.208$ (Schneider et al. 2005). This object has an apparent i-band magnitude $m_i = 15.323$ mag ($M_{1450} \simeq -29.3$ mag), making it the brightest quasar in the SDSS catalog at this redshift (Stern et al. 2015).

Figure 8 displays the resulting profiles with our default observational settings detailed in Section 5, where the electron-scattering signal appears detectable out to ∼150 pkpc. At distances beyond ∼115 pkpc, however, the dust-scattering emission profile overwhelms that from electrons, and the two signals are indistinguishable beyond ∼90 pkpc. The high dust emission level results again from the wavelength dependence of the dust-scattering (absorption) cross-section, and the fact that at $z \simeq 2.2$ we probe bluer rest-frame wavelengths,

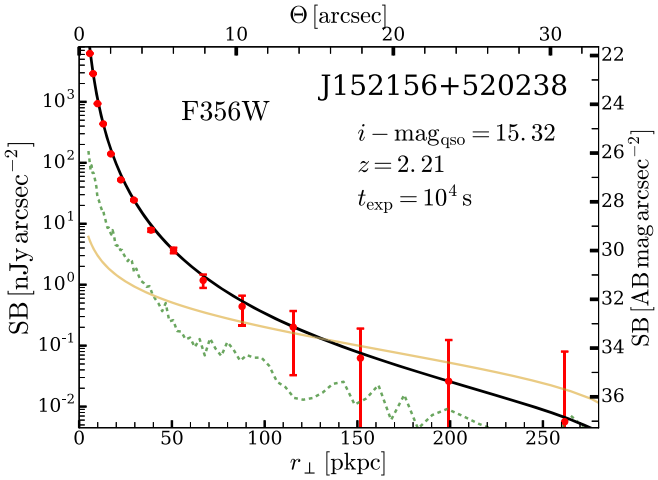

Figure 8. Surface brightness profiles as in Figure 5 but for the $z = 2.208$ quasar SDSS J152156+520238, with an exposure time of ∼3 hr.

∼1.1 μm, than in our fiducial example at $z \simeq 1$ (rest frame ∼1.8 μm; see Figure 5).

According to Figure 6, targeting comparably luminous existing quasars at even higher redshifts ($z > 2$) would imply a still higher S/N for the electron-scattered emission. However, in practice, because the dust optical depth increases toward bluer rest-frame wavelengths, and hence toward higher redshifts in a fixed observed-frame filter, the separation between the electron and dust-scattering signals beyond ∼100 pkpc could be challenging. Dust emission dominates these profiles at distances beyond ∼80 (∼55) pkpc at $z = 3$ ($z = 4$). Note, however, that our calculations implicitly assume that the dust optical depth $\tau_{\rm cool,0} \propto n_{\rm H,cool,0} r_{\rm vir} \propto (1+z)^4$, the same scaling as scattering by electrons in the hot phase, because in our cool gas model, $n_{\rm H,cool,0} \propto (1+z)^3$, just like the electron density $n_{\rm e}$ in the hot phase. While arguments based on gravitational collapse, virialization, and shock-heating imply that the hot-phase density has to increase as $n_e \propto (1+z)^3$, the redshift scaling for the cool-phase gas density is much less clear, given that the physical processes giving rise to the cool gas in the quasar CGM are poorly understood (e.g., Fumagalli et al. 2014; but see Faucher-Giguère et al. 2015). It is thus possible that the cool-phase density does not track the redshift evolution of the mean density of the universe, which would imply significantly lower dust emission at high redshifts. That said, by analyzing observations of multiple filters covering a broad range of rest-frame wavelengths, one should be able to use the wavelength dependence of the signals to determine whether the scattering medium is electrons versus dust, as the former results in extended emission following the SED of the quasar, whereas the latter follows the SED of the quasar multiplied by the reddening law.

7. Discussion

We discuss the limitations and caveats of our proposed formalism in Section 7.1 and alternative observational approaches in Section 7.2.

7.1. Caveats and Limitations

We explore the effects of considering different density gradients, such as that for the CGM of Milky Way-type

galaxies as recently argued by Singh et al. (2018), in Section 7.1.1; discuss the redshift dependence of the electron density in Section 7.1.2; and the possible quasar obscuration and flickering in Section 7.1.3.

7.1.1. The Hot Gas Density Profile in the CGM

Using a Monte Carlo Markov Chain approach applied to the X-ray and tSZ stacking results of Anderson et al. (2015) and Planck Collaboration et al. (2013), respectively, Singh et al. (2018) estimated the electron temperature and gas fraction in the hot CGM phase of massive galaxies at $z = 0.1$–0.2. Assuming a power law, their calculations favor a radial dependence for the electron density of the form $n_e \propto r^{-1.2}$, which implies a power-law index approximately a factor of 2 lower than our adopted value of $\alpha_h = 5/2$. This flatter density profile would result in an overall improvement of the detection of the electron-scattered profile at large radii in our fiducial calculations at $z = 1$. Although the signal decreases in the first few tens of physical kiloparsecs (by a factor of 3–4 at $\sim$40 pkpc), it still remains above that of dust, and the S/N is sufficiently high to allow accurate measurements. Furthermore, the flattening enhances the electron profile by a factor of 5–7 at distances above $\sim$200 pkpc, extending the detected distances from $\sim$100 out to $\sim$150 pkpc.

The differences between the profiles in Singh et al. and those in Nelson et al. might be attributed to the difference in redshift in the two studies, $z \sim 0.1$–0.2 and $z = 2$, respectively, and the different halo masses. Furthermore, one result arises from observations while the other is from simulations. The observation of Thomson-scattering emission and the subsequent modeling of the density profiles will be a useful tool to shed light on these dependencies, as well as for testing the prescriptions included in numerical simulations, especially those concerning complex feedback processes that can affect the properties of the hot halo phase.

7.1.2. The Redshift Dependence of the Electron Density

For the calculation of the redshift evolution of the electron-scattering signal, we have considered that the electron density in the halo scales with redshift in the same way as the mean cosmic density, $(1 + z)^3$. However, several models suggest that the halo evolution can be flatter, accounting for the more effective cooling at high redshifts due to the higher gas densities, which results in larger cool gas fractions (e.g., Maller & Bullock 2004; Sharma et al. 2012). We do not explore further models for the electron density evolution, but it is important to keep these effects in mind for future comparisons with real observations.

7.1.3. Quasar Obscuration or Intermittent Emission

Our calculations assume that the quasar radiation is emitted isotropically but, in reality, quasars are believed to be surrounded by a thick dusty torus that will reduce the flux of UV/optical photons into the quasar CGM by a factor $\Omega/4\pi$, where Ω is the solid angle that is unobscured by dust (e.g., Antonucci 1993; Urry & Padovani 1995; Zakamska et al. 2005). Obscured or Type II quasars represent the cases where the orientation of the object results in the attenuation of the accretion disk and broad-line region from our vantage point, and in general, only radio, X-ray, and IR emission escape the central regions toward the observer. By contrast, UV-bright Type I quasars are cases where the accretion disk and broad-line region are visible from our perspective. The possible obscuration adds uncertainty to the measurement of the baryonic content from electron scattering because it reduces the total flux of UV/optical photons into the CGM, reducing the expected surface brightness profiles. Thus, obscuration effects are degenerate with the determination of electron density. However, the opening angle can be constrained because it is directly related to the fraction of hyperluminous quasars that are obscured, i.e., $f_{\rm obscured} = 1 - \Omega/4\pi$. Observations of low-luminosity quasars suggest a fraction $f_{\rm obscured} = 0.5$, implying an opening angle $\equiv\Omega = 2\pi$ (e.g., Lusso et al. 2013 and references therein), but at high luminosities the opening angle has been debated. Some works argue that the so-called "receding torus effect" implies that the most luminous sources are totally unobscured (e.g., Hönig et al. 2011), while other studies based on number counts of obscured quasars claim that even hyperluminous quasars can suffer from obscuration, although these results are subject to large uncertainties (e.g., Assef et al. 2015).

If quasars only emit their UV/optical radiation into 2π steradians, the surface brightness profiles are reduced by a factor of 2, which does not strongly impact their detectability. This uncertainty affects, however, the interpretation of the observations due to the degeneracy with the electron density. Observations at long wavelengths, $\gtrsim$4 μm, reduce this concern, because these wavelengths are much less sensitive to dust absorption and are essentially emitted isotropically. Furthermore, it may be possible to constrain the opening angle of hyperluminous quasars by studying the Lyα forest around them using background sightlines, exploiting the so-called transverse proximity effect (e.g., Schmidt et al. 2017a, 2017b).

Observations of the diffuse scattered emission around a luminous Type II (obscured) quasar would be interesting because the obscuring torus acts like a natural coronagraph and enables the study of the host halo and scattering signal at distances much closer to the central source. At the rest-frame $\sim$1.8 μm wavelengths considered for our fiducial source at $z \sim 1$, the scattered emission in the central regions of the halo would be reduced by a factor of $\sim$1.5 dex, which represents the flux ratio between a Type I and II quasar at this wavelength (see Figures 2 and 3 in Hönig et al. 2011). At larger distances, the signal would be dominated by the (unobscured) $\sim$1.5 dex brighter radiation emitted in other directions and scattered into our line of sight, although it may be difficult to quantify the Type I luminosity precisely and, therefore, the electron density.

Finally, our calculations assume that the quasars emit their radiation continuously over a sufficiently long timescale that time-delay effects between radiation emitted at the same time but in different directions do not impact our results. The maximum time delay compared to photons emitted directly toward the observer will be for those photons emitted in a direction antiparallel to the line of sight toward the observer and then back-scattered by the electrons. For example, considering scattering off the free electrons at a radial distance of 100 pkpc from the source implies a maximum time delay of 6.5×10^5 yr, twice the crossing time. If quasars flicker on timescales shorter than this (see, e.g., Eilers et al. 2017), time-delay effects must be considered. For the case of dust scattering, the impact of time delay is less significant because most of the observed radiation arises from emission at small

angles from the line of sight. For simplicity, we have not taken into account such effects in our current calculations.

7.2. Ground-based Observations

One of the benefits of considering observations with *JWST* is its compact and stable PSF. In ground-based observations, the subtraction of the PSF is a vital (not simple to achieve) requirement to obtain a detection (de Jong 2008; Trujillo & Bakos 2013; Sandin 2014, 2015). For instance, Hutchings et al. (2004) made use of a coronagraph, together with *HST* data, to support and reinforce their ground-based observations of the host galaxy around the bright 3C 273 quasar. However, ground-based telescopes have larger apertures and are less oversubscribed than space-based facilities, so it is worth discussing observations from the ground. Indeed, if an obscured hyperluminous quasar were identified with intrinsic (unobscured) luminosity comparable to the brightest Type I's, then the obscuring torus acts like a natural coronagraph, and it would be highly interesting to pursue deep observations from the ground.

The level of our predicted surface brightness profiles is challenging but achievable with current 8 m class telescopes. Although the emission profile in Figure 5 is as bright as $\sim$29 mag arcsec^{-2} in the inner regions, it approaches $\sim$32.5 mag arcsec^{-2} at 100 pkpc. Trujillo & Fliri (2016) explored the limits of low surface brightness observations on 8 m class telescopes and reached a surface brightness limit of $\sim$31.5 mag arcsec^{-2} (3σ in a 10×10 arcsec box) in an 8 hr r-band integration. By azimuthally averaging (over annular bins with radii of $\sim 100''$, comparable to the scales we consider here), they were able to probe down to surface brightness levels of $\sim$33 mag arcsec^{-2}, comparable to our signal at 100 pkpc. Also recently, Buitrago et al. (2017) analyzed HUDF data to study elliptical galaxies, and their careful treatment allowed them to reach surface brightness levels of $\sim$31 mag arcsec^{-2}. Future optical instruments, such as those planned for the TMT,[11] GMT,[12] and E-ELT[13] telescopes with apertures of $\sim$30 m, will probe to deeper levels, although at IR wavelengths, observations from the ground will not be competitive with the extremely low surface brightness that can be achieved with *JWST* and its possible space-based successors, such as *LUVOIR*.[14]

Finally, the Dragonfly Telephoto Array[15] (Abraham & van Dokkum 2014) is a novel small ground-based instrument designed to reduce considerably the undesired scattered light in the telescope compared to usual reflective telescopes, which makes it capable of reaching surface brightness levels below $\mu_B = 30$ mag arcsec^{-2} with observations of $\sim$10 hr. Dragonfly is well suited for targeting diffuse and extended structures, and it has already demonstrated its potential for these types of observations (e.g., van Dokkum et al. 2015a, 2015b; Merritt et al. 2016).

8. Conclusion

We have demonstrated the feasibility of observing diffuse electron-scattered radiation from a hyperluminous quasar in the CGM of the host galaxy with *JWST*, which can be used to probe the physical properties of the warm and hot gas, and to quantify the baryonic content in these CGM phases. We have parameterized the central quasar and the radiation sources and gas in the host halo following observational and numerical results. We have calculated the electron- and dust-scattered surface brightness profiles considering the respective scattering redistribution functions and accounted for the radiation from satellites sources, nebular (recombination) radiation, and potential extended stellar halos. Our findings can be summarized as follows:

1. The surface brightness profile of the NIR radiation from a luminous quasar at $z = 1$, scattered by the free electrons in the warm and hot CGM of the host galaxy, is detectable up to $\sim$100 pkpc from the central quasar (at a surface brightness level of $\sim$32.5 AB mag arcsec^{-2}) with less than 3 hr of imaging observations with NIRCam on board the *JWST*. This signal appears above those of dust, recombination, and halo star formation (after masking the brightest satellite sources) and should also be at least a factor of 10 higher than extended stellar halo emission.
2. A positive detection of this electron-scattering signal would provide a direct measurement of the radial profile of the number density of free electrons and, therefore, the amount of baryons in the warm and hot CGM phases in high-redshift halos.
3. The electron-scattering surface brightness is redshift independent, because warm/hot gas is denser at higher redshifts and because the halos are more compact. The detectability of the signal scales as the angular size of the virial radius, which is a very weak function of redshift for $z \gtrsim 1$. This implies that the signal is detectable around hyperluminous quasars out to above 100 pkpc from the central source up to the redshifts of the cosmic reionization at $z \sim 6.5$ with 10^4 s (<3 hr) of observation.
4. At $z \lesssim 1.4$, where quasars are intrinsically much less luminous, extended stellar halos, which have been detected around massive nearby galaxies, could dominate over the electron-scattering signal. For the hyperluminous quasars at $z \gtrsim 1$, however, this signal will be a factor of $\sim$30 lower than the electron-scattering emission.
5. At $z \gtrsim 2.5$, the electron-scattering signal might be contaminated by dust scattering if the density of cool gas in the quasar CGM scales as $\propto (1+z)^3$, similar to expectations for the warm/hot phase. This potential increase in the dust contamination at higher redshift occurs because one probes bluer rest-frame wavelengths, which increases the dust-scattering optical depth relative to the electron-scattering one. However, it may be possible to determine the nature of the scattering medium by analyzing the color of the signal.

Our proposed method of using observations of extended Thomson-scattered radiation from hyperluminous quasars aims to open a new and unique window for subsequent detailed studies of baryons in galactic halos, independent of their temperature, probing the spatial distribution of the predicted warm and hot phases that have been extremely difficult to observe. Furthermore, the presence of hyperluminous quasars out to redshifts as large as $z \sim 6.3$ (Wu et al. 2015), coupled with the redshift independence of the electron-scattering surface brightness (and the weak redshift dependence of the

[11] https://www.tmt.org
[12] http://www.gmto.org/
[13] https://www.eso.org/public/teles-instr/elt/
[14] https://asd.gsfc.nasa.gov/luvoir/
[15] http://www.astro.yale.edu/dragonfly/index.html

S/N), suggests that we may be able to probe halo baryons via electron scattering over 10 billion years of cosmic history, provided that scattering by dust is not a major contaminant. This approach does not suffer from the difficulties and limitations of other techniques that make use of X-rays or the tSZ effect and therefore can be crucial for setting constraints on the impact of quasar feedback, as well as for quantifying the "missing" baryons inhabiting the CGM of massive halos up to the redshifts of cosmic reionization.

While the present work demonstrates that electron-scattering halos should be easily detectable in high-resolution, sensitive *JWST* images, obtaining a spectrum of the diffuse emission would provide important additional information. Because Thomson-scattered photons inherit a Doppler shift determined by the electron velocities, which are moving $\sqrt{m_e/m_p} \sim 40$ faster than the virial velocity, an electron-scattered quasar emission line will be broadened by $\sim 10^4\,\mathrm{km\,s^{-1}}$, which exceeds the intrinsic line widths ($\sim 3000\,\mathrm{km\,s^{-1}}$; Loeb 1998). If this broadening is detectable via a spectrum of the scattered line emission, it opens up the exciting possibility of directly measuring the temperature of baryons in high-redshift halos. Furthermore, these imaging and spectroscopic observations could be complemented with polarimetry, which would definitively prove that scattering is the source of emission, because of the high polarization resulting from scattering off of dust and electrons (e.g., Zakamska et al. 2005 and references therein). We will address these questions in detail in a future paper.

We thank the referee for important comments on the distribution of gas inside halos and its dependence on redshift, which have improved the discussion of our results. The initial inspiration for this work grew out of a stimulating discussion with Ski Antonucci, and we are grateful to him for many valuable and detailed comments on quasars and scattering. We thank Brice Ménard and Yi-Kuan Chiang for their critical comments on extended stellar halos around massive galaxies, and Ignacio Trujillo, Feige Wang, Fabrizio Arrigoni Battaia, and Jonathan Stern for sharing their data/scripts with us. We also thank Gordon T. Richards and J. Stern for helpful discussions about dust in quasar environments; Mark Dijkstra, Avi Loeb, and Sebastiano Cantalupo for noting important radiative processes; and Jordi Miralda-Escudé and Andreu Arinyo-i-Prats for highlighting the impact of potential time-delay effects. The authors are grateful to the scientists at the MPIA in Heidelberg and the members of the UCSB/MPIA ENIGMA group, as well as those at the CCAPP and Astronomy department of the Ohio State University, for their kind hospitality and enriching discussions.

ORCID iDs

Lluís Mas-Ribas https://orcid.org/0000-0003-4584-8841
Joseph F. Hennawi https://orcid.org/0000-0002-7054-4332

References

Abazajian, K. N., Adelman-McCarthy, J. K., Agüeros, M. A., et al. 2009, ApJS, 182, 543
Abraham, R., van Dokkum, P., Conroy, C., et al. 2017, in Outskirts of Galaxies, Astrophysics and Space Science Library, Vol. 434, ed. J. H. Knapen, J. C. Lee, & A. Gil de Paz (Switzerland: Springer International), 333
Abraham, R. G., & van Dokkum, P. G. 2014, PASP, 126, 55
Anderson, M. E., & Bregman, J. N. 2010, ApJ, 714, 320
Anderson, M. E., & Bregman, J. N. 2011, ApJ, 737, 22
Anderson, M. E., Bregman, J. N., & Dai, X. 2013, ApJ, 762, 106
Anderson, M. E., Churazov, E., & Bregman, J. N. 2016, MNRAS, 455, 227
Anderson, M. E., Gaspari, M., White, S. D. M., Wang, W., & Dai, X. 2015, MNRAS, 449, 3806
Antonucci, R. 1993, ARA&A, 31, 473
Antonucci, R., Hurt, T., & Miller, J. 1994, ApJ, 430, 210
Antonucci, R. R. J., & Miller, J. S. 1985, ApJ, 297, 621
Arrigoni Battaia, F., Hennawi, J. F., Cantalupo, S., & Prochaska, J. X. 2016, ApJ, 829, 3
Arrigoni Battaia, F., Hennawi, J. F., Prochaska, J. X., & Cantalupo, S. 2015, ApJ, 809, 163
Arrigoni Battaia, F., Prochaska, J. X., Hennawi, J. F., et al. 2018, MNRAS, 473, 3907
Arrigoni Battaia, F., Yang, Y., Hennawi, J. F., et al. 2014, in IAU Symp. 304, Multiwavelength AGN Surveys and Studies, ed. A. M. Mickaelian & D. B. Sanders (Cambridge: Cambridge Univ. Press), 32
Assef, R. J., Eisenhardt, P. R. M., Stern, D., et al. 2015, ApJ, 804, 27
Bahcall, J. N., Kirhakos, S., Saxe, D. H., & Schneider, D. P. 1997, ApJ, 479, 642
Bahcall, J. N., Kirhakos, S., & Schneider, D. P. 1995, ApJ, 450, 486
Birnboim, Y., & Dekel, A. 2003, MNRAS, 345, 349
Bleem, L. E., Stalder, B., de Haan, T., et al. 2015, ApJS, 216, 27
Bogdan, A., Bourdin, H., Forman, W. R., et al. 2017, arXiv:1710.07286
Bogdán, Á, David, L. P., Jones, C., Forman, W. R., & Kraft, R. P. 2012, ApJ, 758, 65
Bogdán, Á, Forman, W. R., Kraft, R. P., & Jones, C. 2013, ApJ, 772, 98
Borisova, E., Cantalupo, S., Lilly, S. J., et al. 2016, ApJ, 831, 39
Boyle, B. J., Shanks, T., Croom, S. M., et al. 2000, MNRAS, 317, 1014
Boyle, B. J., Shanks, T., & Peterson, B. A. 1988, MNRAS, 235, 935
Bregman, J. N. 2007, ARA&A, 45, 221
Brown, M. J. I., Moustakas, J., Smith, J.-D. T., et al. 2014, ApJS, 212, 18
Buitrago, F., Trujillo, I., Curtis-Lake, E., et al. 2017, MNRAS, 466, 4888
Cai, Z., Fan, X., Yang, Y., et al. 2017, ApJ, 837, 71
Cantalupo, S., Arrigoni-Battaia, F., Prochaska, J. X., Hennawi, J. F., & Madau, P. 2014, Natur, 506, 63
Cardelli, J. A., Clayton, G. C., & Mathis, J. S. 1989, ApJ, 345, 245
Carlstrom, J. E., Holder, G. P., & Reese, E. D. 2002, ARA&A, 40, 643
Cen, R., & Ostriker, J. P. 2006, ApJ, 650, 560
Cen, R., & Safarzadeh, M. 2015, ApJL, 809, L32
Chatterjee, S., Ho, S., Newman, J. A., & Kosowsky, A. 2010, ApJ, 720, 299
Cohen, M. H., Ogle, P. M., Tran, H. D., Goodrich, R. W., & Miller, J. S. 1999, AJ, 118, 1963
Coil, A. L., Hennawi, J. F., Newman, J. A., Cooper, M. C., & Davis, M. 2007, ApJ, 654, 115
Conroy, C., Prada, F., Newman, J. A., et al. 2007, ApJ, 654, 153
Conroy, C., & White, M. 2013, ApJ, 762, 70
Courteau, S., Widrow, L. M., McDonald, M., et al. 2011, ApJ, 739, 20
Courvoisier, T. J.-L. 1998, A&ARv, 9, 1
Crichton, D., Gralla, M. B., Hall, K., et al. 2016, MNRAS, 458, 1478
Dai, X., Anderson, M. E., Bregman, J. N., & Miller, J. M. 2012, ApJ, 755, 107
Decarli, R., Walter, F., Venemans, B. P., et al. 2017, Natur, 545, 457
de Graaff, A., Cai, Y.-C., Heymans, C., & Peacock, J. A. 2017, arXiv:1709.10378
de Jong, R. S. 2008, MNRAS, 388, 1521
Dekel, A., Sari, R., & Ceverino, D. 2009, ApJ, 703, 785
Dey, A., Cimatti, A., van Breugel, W., Antonucci, R., & Spinrad, H. 1996, ApJ, 465, 157
Dirac, P. A. M. 1925, MNRAS, 85, 825
Draine, B. T. 2003, ApJ, 598, 1017
D'Souza, R., Kauffman, G., Wang, J., & Vegetti, S. 2014, MNRAS, 443, 1433
Dutta Chowdhury, D., & Chatterjee, S. 2017, ApJ, 839, 34
Eilers, A.-C., Davies, F. B., Hennawi, J. F., et al. 2017, ApJ, 840, 24
Fabian, A. C. 1989, MNRAS, 238, 41P
Faucher-Giguère, C.-A., Hopkins, P. F., Kereš, D., et al. 2015, MNRAS, 449, 987
Ferland, G. J., Chatzikos, M., Guzmán, F., et al. 2017, RMxAA, 53, 385
Fukugita, M., Hogan, C. J., & Peebles, P. J. E. 1998, ApJ, 503, 518
Fukugita, M., & Peebles, P. J. E. 2004, ApJ, 616, 643
Fumagalli, M., Hennawi, J. F., Prochaska, J. X., et al. 2014, ApJ, 780, 74
Garcia-Vergara, C., Hennawi, J. F., Barrientos, L. F., & Rix, H.-W. 2017, arXiv:1701.01114
Gardner, J. P., Mather, J. C., Clampin, M., et al. 2006, SSRv, 123, 485
Geller, R. M., Sault, R. J., Antonucci, R., et al. 2000, ApJ, 539, 73
Gilfanov, M. R., Syunyaev, R. A., & Churazov, E. M. 1987, SvAL, 13, 233

Gordon, K. D., Clayton, G. C., Misselt, K. A., Landolt, A. U., & Wolff, M. J. 2003, ApJ, 594, 279
Goulding, A. D., Greene, J. E., Ma, C.-P., et al. 2016, ApJ, 826, 167
Gralla, M. B., Crichton, D., Marriage, T. A., et al. 2014, MNRAS, 445, 460
Greco, J. P., Hill, J. C., Spergel, D. N., & Battaglia, N. 2015, ApJ, 808, 151
Gupta, A., Mathur, S., Krongold, Y., Nicastro, F., & Galeazzi, M. 2012, ApJL, 756, L8
Guyon, O., Sanders, D. B., & Stockton, A. 2006, ApJS, 166, 89
Hand, N., Appel, J. W., Battaglia, N., et al. 2011, ApJ, 736, 39
Harrison, C. M. 2017, NatAs, 1, 0165
Hayes, M., Östlin, G., Schaerer, D., et al. 2013, ApJL, 765, L27
Hennawi, J. F., & Prochaska, J. X. 2007, ApJ, 655, 735
Hennawi, J. F., & Prochaska, J. X. 2013, ApJ, 766, 58
Hennawi, J. F., Prochaska, J. X., Burles, S., et al. 2006, ApJ, 651, 61
Hennawi, J. F., Prochaska, J. X., Cantalupo, S., & Arrigoni-Battaia, F. 2015, Sci, 348, 779
Henyey, L. G., & Greenstein, J. L. 1941, ApJ, 93, 70
Hill, J. C., Baxter, E. J., Lidz, A., Greco, J. P., & Jain, B. 2017, arXiv:1706.03753
Hojjati, A., McCarthy, I. G., Harnois-Deraps, J., et al. 2015, JCAP, 10, 047
Holder, G. P., & Loeb, A. 2004, ApJ, 602, 659
Hönig, S. F., Leipski, C., Antonucci, R., & Haas, M. 2011, ApJ, 736, 26
Hu, W., & Kravtsov, A. V. 2003, ApJ, 584, 702
Huang, S., Leauthaud, A., Greene, J., et al. 2017, arXiv:1707.01904
Humphrey, P. J., Buote, D. A., O'Sullivan, E., & Ponman, T. J. 2012, ApJ, 755, 166
Hutchings, J. B. 1982, ApJ, 255, 70
Hutchings, J. B., Stoesz, J., Veran, J., & Rigaut, F. 2004, PASP, 116, 154
Hyvönen, T., Kotilainen, J. K., Falomo, R., Örndahl, E., & Pursimo, T. 2007a, A&A, 476, 723
Hyvönen, T., Kotilainen, J. K., Örndahl, E., Falomo, R., & Uslenghi, M. 2007b, A&A, 462, 525
Khedekar, S., Churazov, E., Sazonov, S., Sunyaev, R., & Emsellem, E. 2014, MNRAS, 441, 1537
Kishimoto, M., Antonucci, R., Cimatti, A., et al. 2001, ApJ, 547, 667
Kitayama, T. 2014, PTEP, 2014, 06B111
Knapen, J. H., & Trujillo, I. 2017, in Outskirts of Galaxies, Astrophysics and Space Science Library, Vol. 434, ed. J. H. Knapen, J. C. Lee, & A. Gil de Paz (Switzerland: Springer International Publishing), 255
Kormendy, J., Fisher, D. B., Cornell, M. E., & Bender, R. 2009, ApJS, 182, 216
Koyama, K., Inoue, H., Tanaka, Y., et al. 1989, PASJ, 41, 731
Krawczyk, C. M., Richards, G. T., Gallagher, S. C., et al. 2015, AJ, 149, 203
Krick, J. E., Glaccum, W. J., Carey, S. J., et al. 2012, ApJ, 754, 53
Lau, M. W., Prochaska, J. X., & Hennawi, J. F. 2016, ApJS, 226, 25
Laursen, P. 2010, arXiv:1012.3175
Le Brun, A. M. C., McCarthy, I. G., & Melin, J.-B. 2015, MNRAS, 451, 3868
Leclercq, F., Bacon, R., Wisotzki, L., et al. 2017, arXiv:1710.10271
Lee, H.-W. 1999, ApJL, 511, L13
Li, A., & Draine, B. T. 2001, ApJ, 554, 778
Li, J.-T., Bregman, J. N., Wang, Q. D., et al. 2017, arXiv:1710.07355
Loeb, A. 1998, ApJL, 508, L115
Lusso, E., Hennawi, J. F., Comastri, A., et al. 2013, ApJ, 777, 86
Lusso, E., Worseck, G., Hennawi, J. F., et al. 2015, MNRAS, 449, 4204
Maller, A. H., & Bullock, J. S. 2004, MNRAS, 355, 694
Mannucci, F., Basile, F., Poggianti, B. M., et al. 2001, MNRAS, 326, 745
Martel, A. R., Ford, H. C., Tran, H. D., et al. 2003, AJ, 125, 2964
Martin, D. C., Chang, D., Matuszewski, M., et al. 2014, ApJ, 786, 106
Martin, D. C., Matuszewski, M., Morrissey, P., et al. 2015, Natur, 524, 192
Mas-Ribas, L., & Dijkstra, M. 2016, ApJ, 822, 84
Mas-Ribas, L., Dijkstra, M., Hennawi, J. F., et al. 2017a, ApJ, 841, 19
Mas-Ribas, L., Hennawi, J. F., Dijkstra, M., et al. 2017b, ApJ, 846, 11
Matsuda, Y., Yamada, T., Hayashino, T., et al. 2012, MNRAS, 425, 878
Matthee, J., Sobral, D., Oteo, I., et al. 2016, MNRAS, 458, 449
McGaugh, S. S., Schombert, J. M., de Blok, W. J. G., & Zagursky, M. J. 2010, ApJL, 708, L14
Ménard, B., Scranton, R., Fukugita, M., & Richards, G. 2010, MNRAS, 405, 1025
Merritt, A., van Dokkum, P., Abraham, R., & Zhang, J. 2016, ApJ, 830, 62
Miller, J. S., & Goodrich, R. W. 1990, ApJ, 355, 456
Momose, R., Ouchi, M., Nakajima, K., et al. 2014, MNRAS, 442, 110
Nelson, D., Genel, S., Pillepich, A., et al. 2016, MNRAS, 460, 2881
Ogle, P. M., Brookings, T., Canizares, C. R., Lee, J. C., & Marshall, H. L. 2003, A&A, 402, 849
Oh, S., Greene, J. E., & Lackner, C. N. 2017, ApJ, 836, 115
Patel, S. G., van Dokkum, P. G., Franx, M., et al. 2013, ApJ, 766, 15
Peek, J. E. G., Ménard, B., & Corrales, L. 2015, ApJ, 813, 7
Pei, Y. C. 1992, ApJ, 395, 130
Persic, M., & Salucci, P. 1992, MNRAS, 258, 14P
Peterson, B. M. 1997, An Introduction to Active Galactic Nuclei (Cambridge: Cambridge Univ. Press)
Planck Collaboration, Ade, P. A. R., Aghanim, N., et al. 2013, A&A, 557, A52
Planck Collaboration, Ade, P. A. R., Aghanim, N., et al. 2016, A&A, 594, A13
Poggianti, B. M. 1997, A&AS, 122, arXiv:astro-ph/9608029
Prescott, M. K. M., Dey, A., & Jannuzi, B. T. 2009, ApJ, 702, 554
Prochaska, J. X., & Hennawi, J. F. 2009, ApJ, 690, 1558
Prochaska, J. X., Hennawi, J. F., & Simcoe, R. A. 2013, ApJL, 762, L19
Prochaska, J. X., & Tumlinson, J. 2009, ASSP, 10, 419
Purcell, C. W., Bullock, J. S., & Zentner, A. R. 2007, ApJ, 666, 20
Richards, G. T., Hall, P. B., Vanden Berk, D. E., et al. 2003, AJ, 126, 1131
Richards, G. T., Lacy, M., Storrie-Lombardi, L. J., et al. 2006a, ApJS, 166, 470
Richards, G. T., Strauss, M. A., Fan, X., et al. 2006b, AJ, 131, 2766
Roche, N., Humphrey, A., & Binette, L. 2014, MNRAS, 443, 3795
Roncarelli, M., Cappelluti, N., Borgani, S., Branchini, E., & Moscardini, L. 2012, MNRAS, 424, 1012
Ruan, J. J., McQuinn, M., & Anderson, S. F. 2015, ApJ, 802, 135
Rybicki, G. B., & Lightman, A. P. 1979, Radiative Processes in Astrophysics (New York: Wiley)
Sandin, C. 2014, A&A, 567, A97
Sandin, C. 2015, A&A, 577, A106
Sarazin, C. L., & Wise, M. W. 1993, ApJ, 411, 55
Sazonov, S. Y., & Sunyaev, R. A. 2000, ApJ, 543, 28
Scannapieco, E., Thacker, R. J., & Couchman, H. M. P. 2008, ApJ, 678, 674
Schmidt, M. 1963, Natur, 197, 1040
Schmidt, T. M., Hennawi, J. F., Worseck, G., et al. 2017a, arXiv:1710.04527
Schmidt, T. M., Worseck, G., Hennawi, J. F., Prochaska, J. X., & Crighton, N. H. M. 2017b, ApJ, 847, 81
Schneider, D. P., Hall, P. B., Richards, G. T., et al. 2005, AJ, 130, 367
Schombert, J. M. 2015, AJ, 150, 162
Sharma, P., McCourt, M., Parrish, I. J., & Quataert, E. 2012, MNRAS, 427, 1219
Sholomitskii, G. B., & Yaskovich, A. L. 1990, SvAL, 16, 383
Shull, J. M., Smith, B. D., & Danforth, C. W. 2012, ApJ, 759, 23
Singh, P., Majumdar, S., Nath, B. B., & Silk, J. 2018, arXiv:1801.06557
Sobral, D., Matthee, J., Best, P., et al. 2016, arXiv:1609.05897
Soldi, S., Türler, M., Paltani, S., et al. 2008, A&A, 486, 411
Spacek, A., Richardson, M., & Scannapieco, E. 2017a, arXiv:1711.05304
Spacek, A., Scannapieco, E., Cohen, S., Joshi, B., & Mauskopf, P. 2016, ApJ, 819, 128
Spacek, A., Scannapieco, E., Cohen, S., Joshi, B., & Mauskopf, P. 2017b, ApJ, 834, 102
Stefanon, M., & Marchesini, D. 2013, MNRAS, 429, 881
Steidel, C. C., Bogosavljević, M., Shapley, A. E., et al. 2011, ApJ, 736, 160
Stern, J., Hennawi, J. F., & Pott, J.-U. 2015, ApJ, 804, 57
Sunyaev, R. A. 1982, SvAL, 8, 175
Sunyaev, R. A., & Zeldovich, Y. B. 1970, Ap&SS, 7, 3
Sunyaev, R. A., & Zeldovich, Y. B. 1972, CoASP, 4, 173
Swetz, D. S., Ade, P. A. R., Amiri, M., et al. 2011, ApJS, 194, 41
Szomoru, D., Franx, M., & van Dokkum, P. G. 2012, ApJ, 749, 121
Tal, T., & van Dokkum, P. G. 2011, ApJ, 731, 89
Tanimura, H., Hinshaw, G., McCarthy, I. G., et al. 2017, arXiv:1709.05024
Temi, P., Brighenti, F., & Mathews, W. G. 2008, ApJ, 672, 244
Trainor, R. F., & Steidel, C. C. 2012, ApJ, 752, 39
Tran, H. D., Cohen, M. H., Ogle, P. M., Goodrich, R. W., & di Serego Alighieri, S. 1998, ApJ, 500, 660
Tripp, T. M., Bowen, D. V., Sembach, K. R., et al. 2004, arXiv:astro-ph/0411151
Trujillo, I., & Bakos, J. 2013, MNRAS, 431, 1121
Trujillo, I., & Fliri, J. 2016, ApJ, 823, 123
Tumlinson, J., Peeples, M. S., & Werk, J. K. 2017, ARA&A, 55, 389
Uchiyama, Y., Urry, C. M., Cheung, C. C., et al. 2006, ApJ, 648, 910
Urry, C. M., & Padovani, P. 1995, PASP, 107, 803
Vanden Berk, D. E., Richards, G. T., Bauer, A., et al. 2001, AJ, 122, 549
van de Voort, F., Quataert, E., Hopkins, P. F., et al. 2016, MNRAS, 463, 4533
van Dokkum, P. G., Abraham, R., Merritt, A., et al. 2015a, ApJL, 798, L45
van Dokkum, P. G., Romanowsky, A. J., Abraham, R., et al. 2015b, ApJL, 804, L26
Veilleux, S., Kim, D.-C., Rupke, D. S. N., et al. 2009, ApJ, 701, 587
Verdier, L., Melin, J.-B., Bartlett, J. G., et al. 2016, A&A, 588, A61
Vernet, J., Fosbury, R. A. E., Villar-Martín, M., et al. 2001, A&A, 366, 7
Wang, F., Wu, X.-B., Fan, X., et al. 2016, ApJ, 819, 24
Wang, L., Viero, M., Ross, N. P., et al. 2015, MNRAS, 449, 4476

Wang, W., & White, S. D. M. 2012, MNRAS, 424, 2574
White, M., Myers, A. D., Ross, N. P., et al. 2012, MNRAS, 424, 933
Wisotzki, L., Bacon, R., Blaizot, J., et al. 2016, A&A, 587, A98
Wu, X.-B., Chen, Z.-Y., Jia, Z.-D., et al. 2010, RAA, 10, 737
Wu, X.-B., Wang, F., Fan, X., et al. 2015, Natur, 518, 512
Xue, R., Lee, K.-S., Dey, A., et al. 2017, ApJ, 837, 172
Yang, Y., Zabludoff, A., Tremonti, C., Eisenstein, D., & Davé, R. 2009, ApJ, 693, 1579
Zakamska, N. L., Schmidt, G. D., Smith, P. S., et al. 2005, AJ, 129, 1212